DEVELOPMENT OF AN ACOUSTO-OPTIC TUNABLE FILTER BASED

TIME-DOMAIN FLUORESCENCE SPECTROMETER

WITH HIGH SCANNING SPEED AND HIGH THROUGHPUT

FOR OPTICAL BIOPSY APPLICATIONS

DEVELOPMENT OF AN ACOUSTO-OPTIC TUNABLE FILTER BASED

TIME-DOMAIN FLUORESCENCE SPECTROMETER

WITH HIGH SCANNING SPEED AND HIGH THROUGHPUT

FOR OPTICAL BIOPSY APPLICATIONS

By

Ji Young Hwang, B.Eng.

A Thesis

Submitted to the School of Graduate Studies

in Partial Fulfillment of the Requirements

for the Degree

Master of Applied Science

McMaster University

MASTER OF APPLIED SCIENCE (2009)   McMaster University

(Engineering Physics)   Hamilton, Ontario

TITLE: DEVELOPMENT OF AN ACOUSTO-OPTIC TUNABLE FILTER BASED

TIME-DOMAIN FLUORESCENCE SPECTROMETER WITH HIGH SCANNING SPEED

AND HIGH THROUGHPUT FOR OPTICAL BIOPSY APPLICATIONS

AUTHOR: Ji Young Hwang, B. Eng. (University of Toronto)

SUPERVISOR: Dr. Qiyin Fang

NUMBER OF PAGES: x, 82

Abstract

In this project, we have developed an acousto-optic tunable filter (AOTF) -based time-resolved fluorescence spectroscopy (AOTF-TRFS) apparatus capable of acquiring fluorescence spectra and lifetimes of biological fluorescent probes with high data acquisition speed required for real-time clinical diagnostics. The system incorporates a non-collinear TeO_2 AOTF, a gated multichannel plate photomultiplier tube (MCP-PMT), a picosecond Nd:YAG pulsed laser, a digital oscilloscope with high sampling rate and a bifurcated fiber optic probe for light delivery and collection. Typically low throughput of the AOTF was enhanced by collecting both first order diffraction beams. The system performance was evaluated by measuring the fluorescence of 9-CA, fluorescein, NADH and FAD. The emission peaks in time-integrated spectra and the retrieved decay lifetimes were in good agreement with literature values over the desired spectral region between 370 nm and 550 nm. The system was able to collect a set of time-resolved fluorescence decay data for a single point site across a 200 nm wavelength range at 5 nm increments within 4 s, which is a significant improvement over the previous generation grating-based instrument.

Acknowledgements

Table of Contents

List of Figures

1. Introduction

There is great interest in developing optical technologies that are capable of performing in situ biomedical diagnosis of pathological conditions without the need for invasive excision and lengthy ex-vivo processing. A wide variety of non- or minimally-invasive optical diagnostic approaches, which may be largely classified into two categories: imaging and spectroscopic modalities, have been investigated. Another category that combines the two modalities is called multi-spectral imaging (MSI) or hyper-spectral imaging (HSI) [1]. For biochemical and medical applications, tissue endogenous fluorescence spectroscopy is one of the most popular and effective research tools among other spectroscopic techniques. Fluorescence generally occurs at lower energies (longer wavelengths) than excitation. If high energy UV excitation light is absorbed by a fluorophore, the emitted fluorescence is usually in the visible range of lower energies. One of the useful properties of fluorescence is that the same emission spectrum is typically observed regardless of excitation wavelength, which is known as Kasha's rule [2]. In this project, we focus on the design and development of one branch of the spectroscopic techniques: time-resolved fluorescence spectroscopy (TRFS).

For detection of tissue abnormality, steady-state fluorescence measurements with its relatively simple and cost-effective instrumentation have extensively been used to acquire fluorescence spectral data of a single tissue site (i.e. point-measurement vs. 2D or 3D imaging)

within a wavelength region of interest. Such measurements are usually performed with continuous illumination and detection. Steady-state spectral data are presented as plots of fluorescence intensity versus wavelength (emission spectra). However, it has been recognized that the intensity decay process of fluorescence contains rich information lost in steady-state measurements. Account has been taken of this problem by introducing time-resolved detection, which measures the time-dependence of fluorescence decay at multiple wavelengths. There are two popular approaches for time-resolved measurements: the time-domain and frequency-domain methods. In time-domain measurements, the time-dependent fluorescence intensity following the excitation pulse is observed and the decay lifetime is calculated from the slope of a plot of log(intensity) versus time. On the other hand, the target can be excited with intensity-modulated light in the frequency-domain method and the time delay (phase angle) of the emission relative to the modulated excitation and the modulation ratio are measured to calculate the lifetime of fluorescence [2]. The time-domain method is preferred in our project because it generally enables the detection system to be highly sensitive and to effectively reject unwanted light. Time-domain measurement has the capability of revealing the aforementioned steady-state information by simply integrating the time-dependent intensity over the decay time, plus differentiation of lifetimes of multiple co-localized fluorophores. When different types of fluorophores with overlapping spectra are present within tissue, a steady-state spectrum, which

simply presents the overall optical signal intensity dependent on a weighted average of multiple

decay times at each wavelength, is often unable to provide practical information for effective

tissue diagnosis. The time-resolved method enhances discrimination among spectrally

overlapping fluorescent probes with distinct fluorescence decays by recording changes in

fluorescence lifetime as a function of wavelength and also improves the signal-to-noise ratio

(SNR) by differentiating the real signal of interest from background noise [2]. In addition,

comparing to steady-state spectral data, fluorescence lifetime is almost irrespective of excitation

or emission intensity variations and can also be indicative of micro-environment (pH, ion

concentration and binding, enzymatic activity, temperature) of the sample. In other words, the

time-resolved method allows significantly improved specificity and robustness of fluorescence

measurements [3].

In spite of these notable strengths, time-resolved fluorescence spectroscopy has not

been widely used in clinical settings due to several obstacles. While steady-state fluorescence

spectroscopy can be implemented in a relatively simple fashion, nanosecond time-resolved

measurements typically require complex and expensive instrumentation. To acquire time-

dependent intensity decay data in the time-domain scheme, a pulsed excitation source is used

whereas a cheaper continuous light source is sufficient for the steady-state method. The width of

the excitation pulse is limited by consideration of the nanosecond scale emission lifetimes of the

probes and the photon detection has to be properly gated [2]. Moreover, the difficulties include long data acquisition time impractical for real-time diagnosis, small dynamic range and low SNR. While time-correlated single-photon counting (TCSPC) technique can ensure high resolution, sensitivity and dynamic range, its data acquisition takes excessively long for clinical settings. High-speed time-gated cameras may offer faster data acquisition speed but they are disadvantaged with regard to dynamic range and SNR [3]. The objective of our project was to at least partly overcome these shortcomings of other time-resolved techniques. In this project, we report the design and development of a compact rapid-scanning solid-state acousto-optic tunable filter (AOTF) based apparatus for in situ time-resolved laser-induced fluorescence spectroscopy (tr-LIFS) of biological systems.

The 1st generation compact tr-LIFS apparatus is shown in Figure 1.1. It typically took 40 s for the grating-based system to collect a complete set of time-resolved fluorescence decay data for a single point site across a 200 nm wavelength range at 5 nm increments [3]. Since scanning the grating of the monochromator, which directly limits the system's data acquisition speed, is generally considered too slow for practical clinical applications, the spectrometer had to be equipped with an auxiliary mode of operation that uses an ICCD camera capable of rapid scan-free single-shot acquisition of spectra for a quick preview of the overall steady-state spectral emission characteristics of fluorescent targets. However, an ICCD camera does not

function effectively under continuous light environment.

(a)

(b)
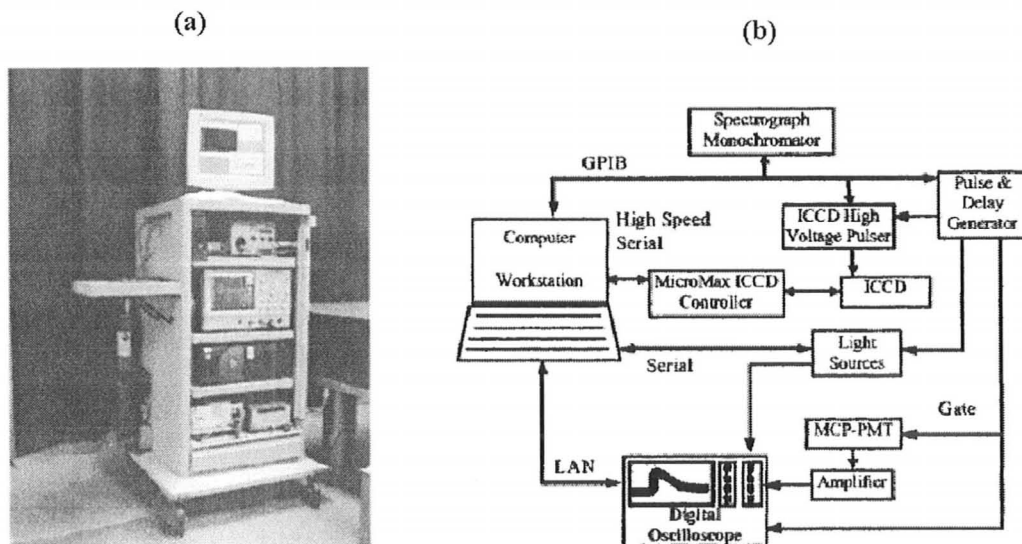
Fig. 1.1. (a) Photograph of the 1st generation tr-LIFS system hosted in a mobile cart; and (b) schematic diagram illustrating the communication scheme of the system [3].

With the aim to improve data acquisition speed of tr-LIFS while maintaining high throughput, the next generation model developed in this project takes advantage of the AOTF technology replacing the task of grating-based devices. AOTFs have been given attention as a convenient, light and high speed means of optical bandpass filtering. These solid-state elasto-optic filters make use of anisotropic Bragg diffraction of light generated by acoustic waves in a birefringent crystal to diffract a narrow bandpass with a central wavelength of interest from broadband incident light. A birefringent crystal in an AOTF is bonded to a piezoelectric transducer, which is excited by applied radio frequencies (RF) and produces acoustic waves in the crystal. The propagating acoustic waves alternately compress and relax the crystal lattice,

establishing a periodic modulation of the density and refractive index within the crystal medium

via the elasto-optic effect. A select group of photons that satisfy proper momentum matching

conditions are diffracted via interaction with phonons created in the crystal. In other words, the

modulation of the index of refraction acts like a transmission diffraction grating. Unlike a

monochromator, however, a solid-state AOTF offers the benefit of having no moving parts and

therefore no restriction is imposed on its temporal performance by any mechanical movements.

The wavelength switching is implemented by varying the radio frequency (RF) applied to a

crystal inside the AOTF. This process can happen within hundreds of ns to a few μs. Therefore,

an AOTF can be scanned or tuned to any wavelength within its operating range at extremely

high rates without the possibility of gear backlash or other mechanical problems that can happen

in a monochromator [1, 4, 5]. With our new system, we were able to witness significant

reduction of data acquisition time to less than 4 s for a 200 nm wavelength range at 5 nm

increments [6]. One of the general downsides of utilizing an AOTF is attributed to its relatively

low throughput. We address this issue by choosing tellurium dioxide (TeO_2) for the birefringent

crystal and using both 1st order diffraction beams.

In the next chapter, the optical design aspect of the AOTF spectrometer unit is

elaborated. Chapter 3 focuses on design considerations for each system component and how

they are put together and synchronized for data acquisition. Chapter 4 explains the

characteristics of the system performance. Finally, important improvements and findings are

discussed in Chapter 5.

References

1. T. Vo-Dinh, B. Cullum and P. Kasili, *Development of a multi-spectral imaging system for medical applications*, Journal of Physics D: Applied Physics, **36**, 1663-1668 (2003).

2. J. R. Lakowicz, *Principles of fluorescence spectroscopy*, 3rd ed., Springer (2006).

3. Q. Y. Fang, T. Papaioannou, J. A. Jo, R. Vaitha, K. Shastry, and L. Marcu, *Time-domain laser-induced fluorescence spectroscopy apparatus for clinical diagnostics*, Review of Scientific Instruments, **75** (1), 151-162 (2004).

4. L. Bei et al., *Acousto-optic tunable filters: fundamentals and applications as applied to chemical analysis techniques*, Progress in Quantum Electronics, **28**, 67-87 (2004).

5. I. C. Chang, *Acousto-optic devices and applications*, Transactions on sonics and ultrasonics, **su-23**, 2-22 (1976).

6. Y. Yuan et al., *High-throughput acousto-optic-tunable-filter-based time-resolved fluorescence spectrometer for optical biopsy*, Optics Letters, **34** (7), 1132-1134 (2009).

2. AOTF Spectrometer

As mentioned earlier, the acousto-optic effect is based on the variation of the refractive index of a medium due to the presence of sound waves in that medium. Only a select group of photons that adhere to certain momentum criteria is diffracted via interactions with the phonons created by high frequency acoustic field applied to the medium. In general, only the first order diffraction maximum is used in acousto-optic devices where Bragg diffraction is preferable due to lower optical losses. The acousto-optic requirements for Bragg diffraction limit the frequency range of acousto-optic interaction.

. The progresses in laser, crystal growth and high frequency piezoelectric transducer technologies have brought the wide availability of acousto-optic devices. There are three main categories of acousto-optic applications; modulators, deflectors and filters. In a modulator, properties of the optical wave are modulated by changing the amplitude, phase, frequency or polarization of the acoustic wave. In the operation of an acousto-optic deflector, the acoustic frequency is varied to deflect the optical beam to different angular positions. The operating principle of acousto-optic filters is based on the fact that the wavelength of the diffracted light is dependent on the acoustic frequency. Acousto-optic tunable filters, abbreviated as AOTFs, can act as optical bandpass filters that are tunable by varying the applied acoustic frequency. There exist two types of AOTFs depending on geometry of acousto-optic interaction; collinear and

8

non-collinear filters. In a collinear AOTF, incident light and the acoustic wave interact collinearly within the medium to produce a coupled diffracted wavefront that is also collinear to the input beam. Therefore, a polarizer is used to separate two orthogonal polarizations (ordinary and extraordinary beams). In a non-collinear AOTF, however, a selected narrow spectral bandwidth is angularly deflected away from the incident beam so that the incident and diffracted beams are physically separated and there is no need for polarizers [1].

2.1. Applications of AOTF technology

AOTFs possess many distinctive attributes that lend themselves to a variety of applications such as wavelength selection and optical imaging. The central wavelength of the diffracted light can be continuously tuned over a wide frequency range by the choice of the acoustic frequency, and the wavelength switching speed can be in tens of microseconds. The main advantages of the AOTF approach include fast tuning speed, tunability of the wavelength and the bandwidth, and control of the intensity of transmitted light. Also, these solid-state devices have no moving parts, which lead to robustness of use. AOTFs have been used for various types of spectrometry mainly in biomedical and chemical settings. However, their low throughput with randomly polarized incident light has hindered their possibly wider applications. With a non-collinear device, the maximum efficiency for the total incoming unpolarized white light drops to half of the values with polarized input light since it is the usual practice to monitor

either of the two first order diffraction beams [1].

Large optical apertures, high spatial resolution and fast tuning capabilities of AOTFs make them versatile tools for spectrally selective imaging applications as well. The use of AOTFs for rapidly tunable multispectral imaging has been pioneered by Farkas and his co-workers [2]. The configuration involves collimating the radiation from a luminescent or illuminated object, directing the radiation through an AOTF tuned to the frequency corresponding to the wavelength of interest, and refocusing the single wavelength image upon an array detector such as CCD [1]. Image blur encountered using AOTF, however, has limited the use of this technique.

2.2. Basic Operating Principles of TeO$_2$ AOTF Devices

It is an important cornerstone to scrutinize the characteristics of the AOTF of our choice for further discussions. The AOTF used in our study was purchased from Brimrose Corporation, Baltimore, MD (part no.: TEAF5-0.36-0.52-S, serial no.: 0610-AO-7358). According to the manufacturer [3], the AOTF's angular aperture is 4 ~ 5 degrees and its separation angle is 6.4 ~ 6.5 degrees. The recommended working spectral range is 360 ~ 520 nm. In this AOTF, the birefringent material, which gives a rise to decomposition of a ray of light into two rays (the ordinary ray and the extraordinary ray), is tellurium oxide (TeO$_2$) that is a left-handed rotating positive uniaxial crystal. It is known that materials with high density and slow

acoustic velocities produce high density and well-defined acoustic waves. The degree of this

observation can be quantified by acousto-optic figures of merit. TeO$_2$ is often chosen as a

birefringent material for AOTFs because of its very high figures of merit, one of which can be

defined as the following [4].

$$M_2 = \frac{n_o{}^3 n_e{}^3 p^2}{\rho v^3}$$

[Eq. 2.1.]

where n_o = refractive index for ordinary light,

n_e = refractive index for extraordinary light,

p = effective photoelastic coefficient,

ρ = density,

v = acoustic velocity.

Since the difference in refractive indices for ordinary rays (o-rays) polarized perpendicular to

the axis of anisotropy of the crystal and extraordinary rays (e-rays) polarized parallel to the axis

is relatively large for TeO$_2$, it is convenient to produce a non-collinear device where diffracted

beams diverge from the undiffracted beam. The main principle of non-collinear AOTF operation

formulated by Chang is that non-collinear diffraction occurs under the so-called non-critical

phase matching (NPM) condition where the tangents to the incident and to the diffracted light

wavevector loci are parallel, which means their group velocities are collinear [4]. Figure 2.1.

schematically illustrates the operating principle of a non-collinear AOTF.
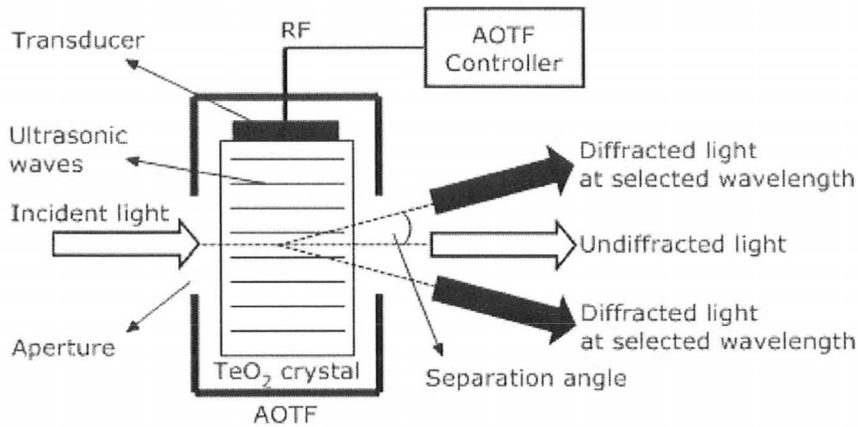
Fig. 2.1. Operation of a non-collinear AOTF. Two first order diffraction beams diverge from the undiffrated beam collinear with the incident beam.

The manufacturer confirmed us that the performance of our AOTF was designed and optimized for NPM in the extraordinary to ordinary path (+1 order) rather than symmetric operation employed in this project. Therefore the spectral resolution in the +1 order is higher than the -1 order which will exhibit broader spectral bandpass. In addition, two first orders will have slightly different central wavelengths from each other for the same applied RF.

It is also worth being aware that TeO_2 has a large optical rotatory power. TeO_2 is a chiral crystal whose molecules are arranged in a spiral configuration. In such a medium, left-circularly and right-circularly polarized light propagate with different phase velocities, which induces birefringence by optical activity. This effect should only be considered when the light propagation direction is near the optical axis. The effect of optical activity on birefringence is known to be significantly reduced when light rays propagate at large off-axis angles. For typical non-collinear AOTF designs, the incident angle is big (~20° or greater). Therefore, the optical

activity has a negligible effect on the tuning relations of such AOTFs. In this case, only the

birefringence caused by a refractive index difference between ordinary and extraordinary rays

needs to be taken into account in the design [5]. The polarization directions for electromagnetic

waves can be visually indicated by an index ellipsoid where the optic axis (Z) and the index

vector (n) in the wave propagation direction are present as in Figure 2.2. Using the wave vector

diagram (Figure 2.3.) based on the index surface of TeO_2, one can determine the polarization

transformations. A complete geometric configuration of the AOTF was constructed in Figure 2.4.

In our model, the angle between the optic axis and the direction perpendicular to the crystal

surface is as big as 16.5° (θ_i) and the angle between the optic axis and the acoustic phase vector

is about 97° (θ_a). The acoustic walk-off is about 73°.
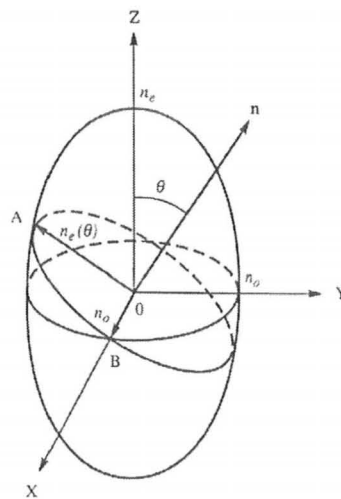
Fig. 2.2. Index ellipsoid of a positive uniaxial crystal [6]. Index vector n is in the incident light wave propagation direction. Refractive index for ordinary light is constant while refractive index for extraordinary light is a function of the angle between index vector and optic axis of the crystal.
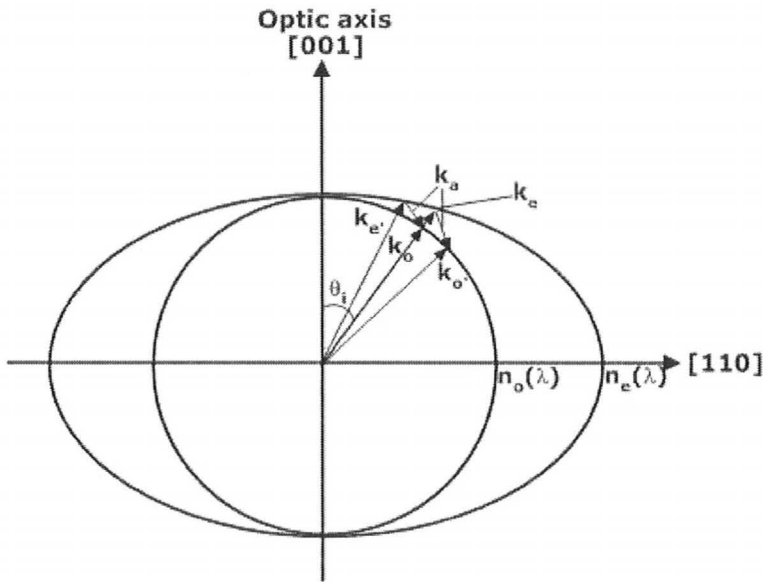
Fig. 2.3. Wavevector diagram for acousto-optic interaction in the non-collinear TeO_2 AOTF. k_e and $k_{e'}$ are input and output e-light wavevectors while k_o and $k_{o'}$ are input and output o-light wavevectors, respectively. k_a is acoustic wavevector. Technically, the geometry of the diagram is subject to incident wavelength as indices of refraction have spectral dependence. Proportions of the diagram were exaggerated for clarity.
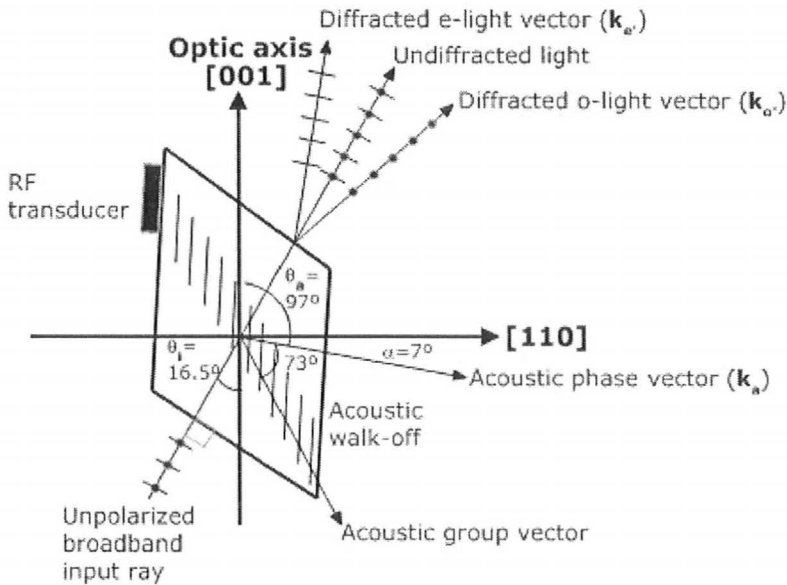
Fig. 2.4. Geometric configuration of the non-collinear TeO_2 AOTF. θ_i is the angle of incidence when the propagation direction of incident beam is normal to the crystal surface.

14

An AOTF controller unit (serial no.: 0610-AE-7359, Figure 2.5.) was provided with its

controlling software (SPF II Driver ver. 1.4.0, Figure 2.6.).
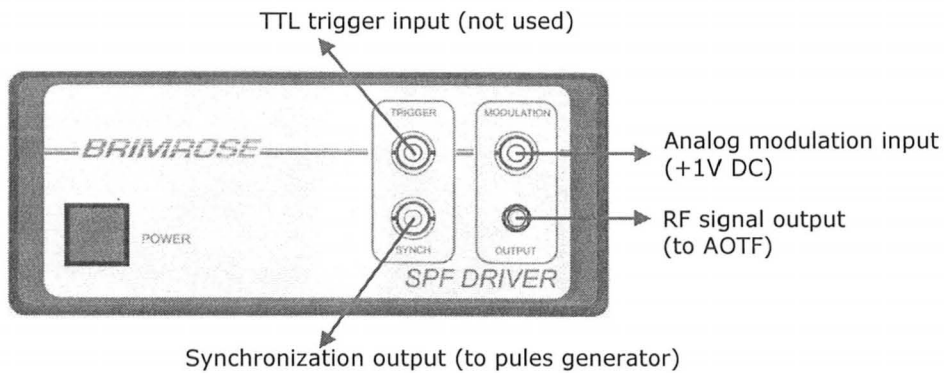
Fig. 2.5. The front of AOTF controller.
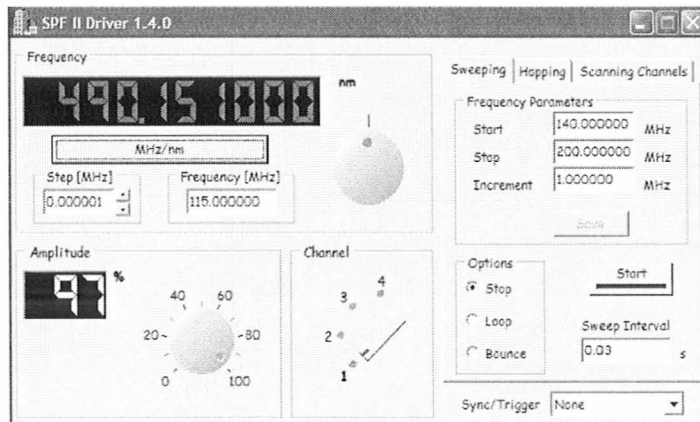
Fig. 2.6. Interface of the AOTF controlling software provided by the manufacturer.

There are two modes of operation for AOTF scanning. In sweeping mode, the driver

allows the user to sweep the frequency linearly by setting the values of "start, "stop", and

"increment" for the channel. The user can specify the duration of each step in the frequency

sweep. The minimum interval for linear frequency sweeping is about 30 μs. In hopping mode,

the frequency change does not have to be linear. The scanning sequence follows a table for each

pair of frequency and corresponding amplitude values that are defined by the user. The scan can

be done by either the PIC microcontroller or the PC depending on the time interval [3].

2.3. Dual Arm AOTF Setup

Randomly polarized fluorescence typically provides too weak signals for AOTFs to

produce reliable information. It is highly necessary to pursue the highest possible throughput of

the AOTF. Comparing to grating-based monochromators, AOTF technique is not typically used

in spectroscopy mainly due to its limited operating spectrum and low throughput (~40%) for

randomly polarized light [1]. In this study, we have implemented a novel "dual arm" design that

uses both first order diffracted beams to double the overall throughput. Since the AOTF in our

system is optimized for only one diffraction order, however, it was expected that using both

diffraction beams would give a rise to broadening of the spectral bandwidth.

The AOTF spectrometer module has several components that have been carefully

chosen. The emission light from the optical fiber is collimated by a plano-convex lens and

diffracted by the AOTF crystal to which acoustic frequencies are applied. Reflected excitation

light is effectively prevented from entering the AOTF by a longpass filter which provides a

sharp cut-off below 355 nm. The AOTF diffraction efficiency and bandpass are greatly affected

by the collimation state of incident light. A couple of concave mirrors reflect both first order

diffracted beams from the AOTF to the 10 mm diameter photocathode effective area of the

microchannel plate photomultiplier tube (MCP-PMT). In this section, the optical characteristics

of each component are analyzed and the issues involved in arranging them are discussed.
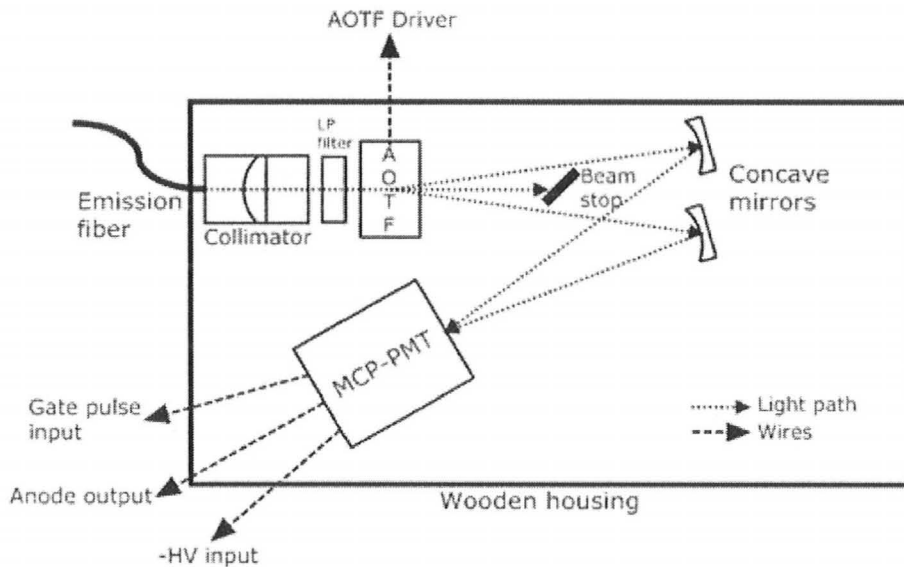
Fig. 2.7. Schematic of the AOTF spectrometer unit.
The finely dotted lines show the paths of light.

2.3.1. Collimator

The diverging output light from the emission fiber needs to be collimated prior to

entering the AOTF aperture to ensure high performance. Collimation is the act of converting the

diverging output from a waveguide into a parallel beam. This process is done by placing the

distal face of the waveguide at the focal plane of a collimating lens. Practically speaking, there

can be no perfectly collimated beam since every beam will spread out after traveling a sufficient

distance [7]. It was recognized that a 25 mm focal length plano-convex lens (25 mm diameter,

over 95% transmission in 370~550 nm, model: 45098, Edmund Optics, Barrington, NJ) can

provide reasonably compromised quality of collimation after comparing rough collimation

profiles of several lenses with different focal lengths. The collimating lens was arranged so that

a collimated beam enters the AOTF optical aperture (5 mm × 6 mm) approximately 3 inches

away from the lens (refer to Figure. 2.9.).
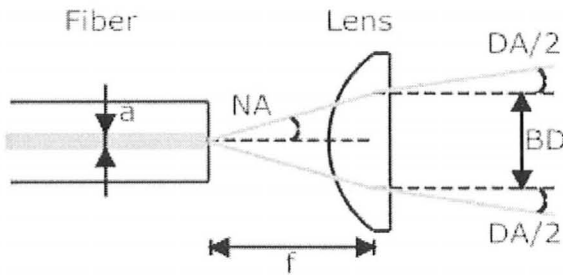
Fig. 2.8. Schematic of fiber collimation. (a = multi-mode fiber core diameter, f = focal length of the lens, NA = numerical aperture of the optical fiber, DA = divergence angle of the collimated beam, BD = collimated beam (core) diameter)
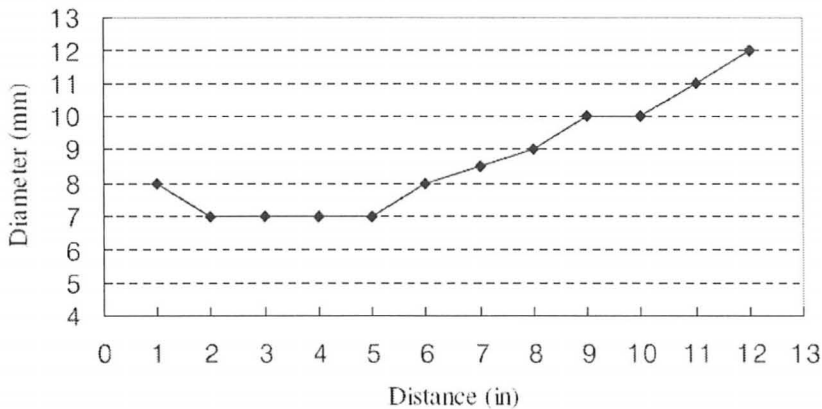
Fig. 2.9. "Collimated" beam diameter (not BD in Fig. 2.8.) vs. distance from the selected lens. The beam diameter was visually measured on a piece of white paper at each distance for comparative and qualitative profile comparisons.

It is possible to obtain a quick estimation of the collimation parameters in the following manner (refer to Figure 2.8.).

$$BD \text{ (beam diameter, mm)} = 2 \times f(mm) \times NA = 2 \times 25mm \times 0.12 = 6mm \qquad \text{[Eq. 2.2.]}$$

$$DA \text{ (full divergence angle, mrad)} = \frac{a\,(\mu m)}{f\,(mm)} = \frac{900\,\mu m}{25mm} = 36mrad = 2° \qquad \text{[Eq. 2.3.]}$$

where a is the mode field diameter and f is the focal length of the lens.

In multi-mode fibers, the core diameter can be considered the mode field diameter, a. [7]. For simplicity of the estimation, the bundle was considered to be a single fiber and the whole bundle diameter (900 µm) was taken as the value of a. The main challenge with our collimation lies in the fact that the collective bundle diameter is considerably large and if the parameter BD is reduced by using a lens with a shorter focal length, the divergence angle increases on the other hand. Moreover, the output bundle is, in fact, consisted of 12 fibers with 12 different axes of divergence slightly displaced from one another, which contributes to the difficulties in effective collimation.

2.3.2. Long Pass (LP) Filter

A long-pass filter (LP02-355RU, Semrock, Rochester, NY) was placed before the entrance window of the AOTF to block the backscattered excitation light at 355 nm. According to the manufacturer, the filter's transmission drops sharply right below 355 nm while it maintains over 95% transmission at longer wavelengths as shown in the curves below.
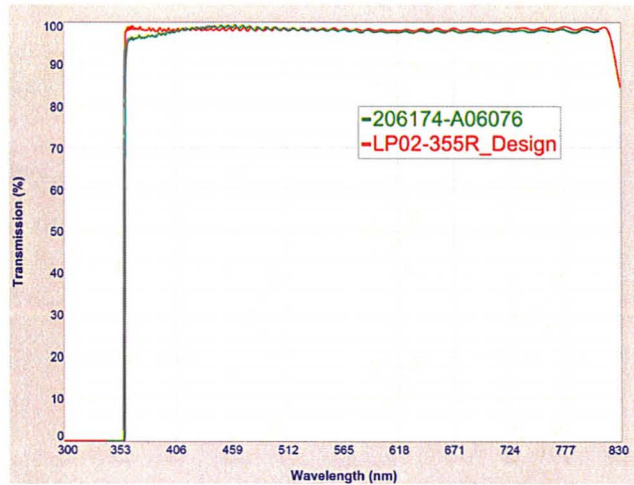
(a)
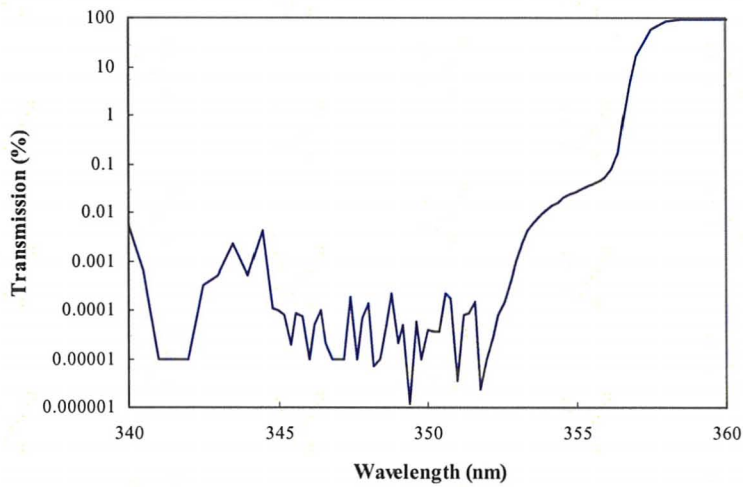
(b)

Fig. 2.10. Transmission spectrum of the long pass filter (LP02-355RU) measured by Semrock.
(a) full spectrum (green curve); (b) near the cut-off wavelength.

2.3.3. Concave Mirrors

Two highly reflective concave mirrors with 150 mm focal length and half an inch

diameter were used to collect both first order beams and focus them to the photo detector. The

20

relative locations of the AOTF, the two concave mirrors, and the photodetector are shown in

Figure 2.11. The divergence angle of the beams was roughly found to be about 2.25°. Since the

sampling frequency of the digital oscilloscope is 40 GHz, the optical path length difference

between the two diffraction beams needs to be below 15 mm (or 50 ps, 3×10^8 m/s = 15mm/50ps)

in order to avoid significant broadening of the signal. In Figure 2.11., the path length difference

is only about 11 mm. The proper focal length of the concave mirrors to reflect diffraction beams

to the photosensitive area of the PMT was estimated using the matrix method in paraxial optics

in the following [8].
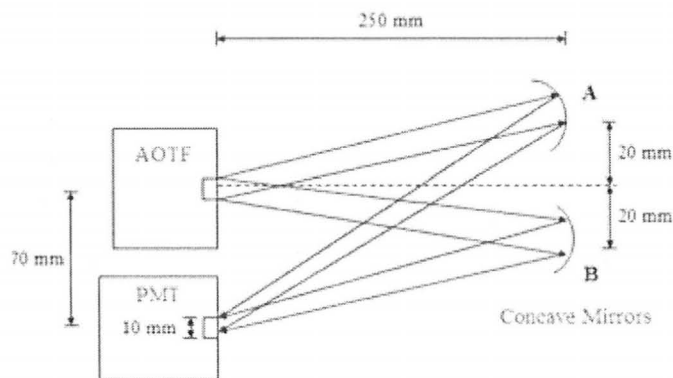
Fig. 2.11. Paths of first order diffraction beams and relative positions of components before arrangement optimization. The difference in path lengths in this arrangement is about 11 mm. The mirrors are denoted as A and B.

In the paraxial approximation, changes in height and direction of a light ray can be

described by linear equations put in matrices. Each beam is thought to be consisted of infinitely

many rays. First, various angles are defined with respect to the axis of symmetry (or the optical

axis) of each mirror as shown in Figure 2.12. The solid arrows represent the propagation of

central rays of the diffracted beams. The arrows in Figure 2.13. trace the outmost rays of each

diffraction beam reflected off the concave mirrors. In Figure 2.14., L is defined as the length by

which the reflected light rays are translated along the axes of symmetry of the mirrors.
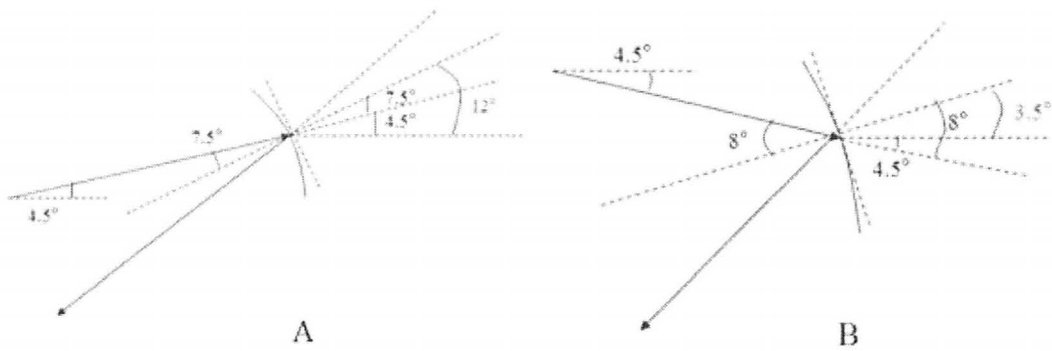
Fig. 2.12. Orientation of mirror A and B. Angles with respect to the axis of symmetry are shown. The curves are mirror surfaces and solid arrows are the central trace of first order diffraction beams.
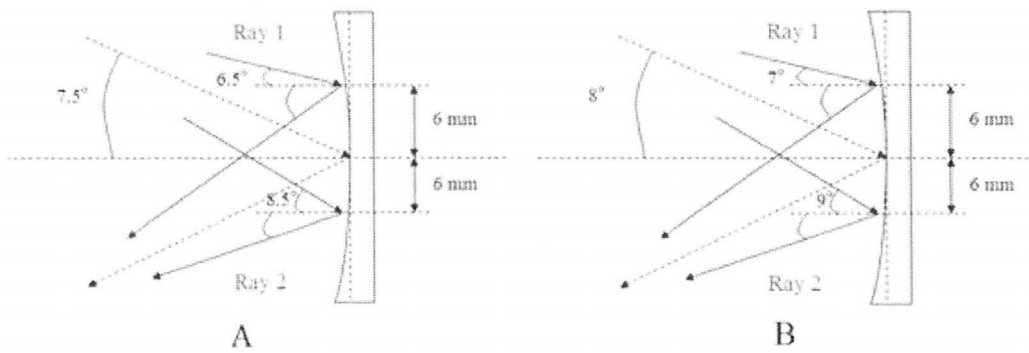
Fig. 2.13. Reflection on mirror A and B. The outmost ray traces of each diffraction beam are shown as solid arrows.
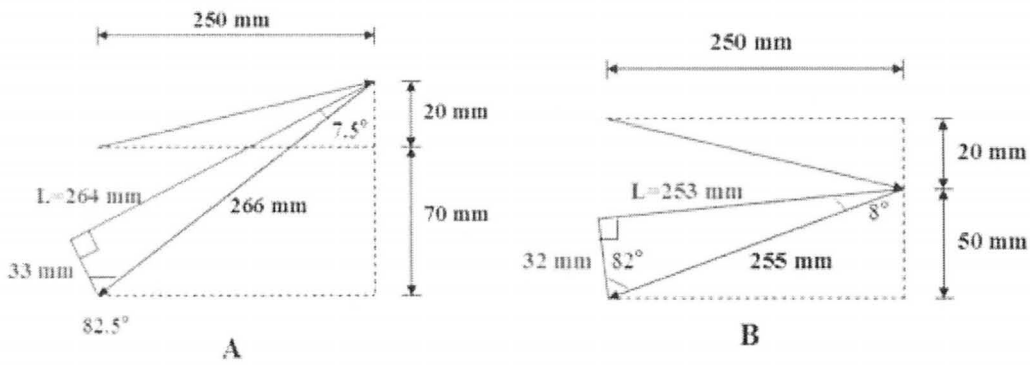
Fig. 2.14. L is defined as the length by which the reflected light rays are translated along the axes of symmetry of the concave mirrors.

The matrix method is used to estimate the state of the outmost rays arriving at the PMT. Let y' and α' be the final height and slope angle relative to the optical axis and y and α be the initial height and slope angle, respectively. The sign for each slope angle is assigned by the sign convention shown in Figure 2.15. Two events, reflection at the mirror surface and translation along the optical axis, for each ray are expressed as 2×2 matrices and incorporated into matrix equations as below. R is the radius of curvature and f is the focal length of the mirrors.
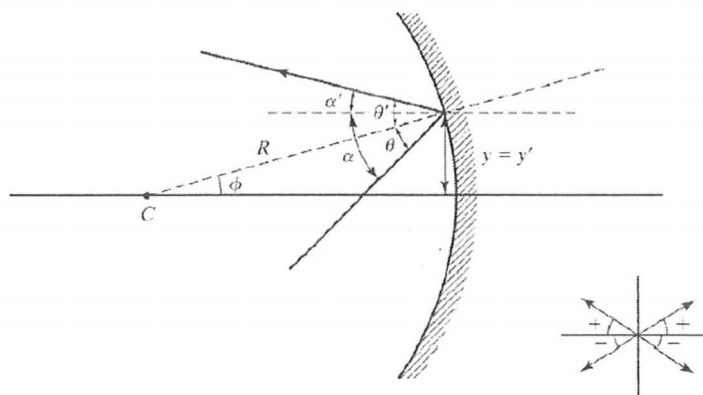
Fig. 2.15. Reflection of a light ray at a concave surface.
The inset illustrates the sign convention for ray angles.

For <u>mirror A</u>,

<u>Ray 1</u> (Fig. 2.13.):

$$\begin{bmatrix} y' \\ \alpha' \end{bmatrix} = \begin{bmatrix} 1 & L \\ 0 & 1 \end{bmatrix}\begin{bmatrix} 1 & 0 \\ 2/R & 1 \end{bmatrix}\begin{bmatrix} y \\ \alpha \end{bmatrix} = \begin{bmatrix} 1 & 264 \\ 0 & 1 \end{bmatrix}\begin{bmatrix} 1 & 0 \\ 2/R & 1 \end{bmatrix}\begin{bmatrix} 6 \\ -0.11 \end{bmatrix} \qquad \text{[Eq. 2.4.]}$$

$$y' = 6 + 264\left(\frac{12}{R} - 0.11\right) \text{[mm]} \qquad \alpha' = \frac{12}{R} - 0.11 \text{ [rad]}$$

$$-38 \langle\ y' = 6 + 264\left(\frac{12}{R} - 0.11\right) \langle\ -28$$

Radius of curvature: $-637mm \langle\ R \langle\ -212mm$

Focal length: $106mm \langle\ f = -\dfrac{R}{2} \langle\ 319mm$

<u>Ray 2</u>:

$$\begin{bmatrix} y' \\ \alpha' \end{bmatrix} = \begin{bmatrix} 1 & L \\ 0 & 1 \end{bmatrix}\begin{bmatrix} 1 & 0 \\ 2/R & 1 \end{bmatrix}\begin{bmatrix} y \\ \alpha \end{bmatrix} = \begin{bmatrix} 1 & 264 \\ 0 & 1 \end{bmatrix}\begin{bmatrix} 1 & 0 \\ 2/R & 1 \end{bmatrix}\begin{bmatrix} -6 \\ -0.15 \end{bmatrix} \qquad \text{[Eq. 2.5.]}$$

$$y' = -6 + 264\left(-\frac{12}{R} - 0.15\right) \text{[mm]} \quad \alpha' = -\frac{12}{R} - 0.15 \text{ [rad]}$$

$$-38 \langle\ y' = -6 + 264\left(-\frac{12}{R} - 0.15\right) \langle\ -28$$

Radius of curvature: $-417mm \langle\ R \langle\ -180mm$

Focal length: $90mm \langle\ f = -\dfrac{R}{2} \langle\ 209mm$

Thus, the common range for both rays is $106mm \langle\ f \langle\ 209mm$ [criterion 1]

And for <u>mirror B</u>,

<u>Ray 1</u>:

$$\begin{bmatrix} y' \\ \alpha' \end{bmatrix} = \begin{bmatrix} 1 & L \\ 0 & 1 \end{bmatrix}\begin{bmatrix} 1 & 0 \\ 2/R & 1 \end{bmatrix}\begin{bmatrix} y \\ \alpha \end{bmatrix} = \begin{bmatrix} 1 & 253 \\ 0 & 1 \end{bmatrix}\begin{bmatrix} 1 & 0 \\ 2/R & 1 \end{bmatrix}\begin{bmatrix} 6 \\ -0.12 \end{bmatrix} \qquad \text{[Eq. 2.6.]}$$

$$y' = 6 + 253\left(\frac{12}{R} - 0.12\right) \text{[mm]} \qquad \alpha' = \frac{12}{R} - 0.12 \text{ [rad]}$$

$$-37 \langle \ y' = 6 + 253\left(\frac{12}{R} - 0.12\right) \langle \ -27$$

Radius of curvature: $-1149mm \ \langle \ R \ \langle \ -240mm$

Focal length: $120mm \ \langle \ f = -\dfrac{R}{2} \ \langle \ 575mm$

Ray 2:

$$\begin{bmatrix} y' \\ \alpha' \end{bmatrix} = \begin{bmatrix} 1 & L \\ 0 & 1 \end{bmatrix}\begin{bmatrix} 1 & 0 \\ 2/R & 1 \end{bmatrix}\begin{bmatrix} y \\ \alpha \end{bmatrix} = \begin{bmatrix} 1 & 253 \\ 0 & 1 \end{bmatrix}\begin{bmatrix} 1 & 0 \\ 2/R & 1 \end{bmatrix}\begin{bmatrix} -6 \\ -0.16 \end{bmatrix} \qquad \text{[Eq. 2.7.]}$$

$$y' = -6 + 253\left(-\frac{12}{R} - 0.16\right) \text{[mm]} \quad \alpha' = -\frac{12}{R} - 0.16 \text{ [rad]}$$

$$-37 \langle \ y' = -6 + 253\left(-\frac{12}{R} - 0.16\right) \langle \ -27$$

Radius of curvature: $-321mm \ \langle \ R \ \langle \ -156mm$

Focal length: $78mm \ \langle \ f = -\dfrac{R}{2} \ \langle \ 161mm$

The common range for both rays is, $120mm \ \langle \ f \ \langle \ 161mm$ [criterion 2]

Comparing the two criteria (criterion 1 and 2) for mirror A and B, to use the same type of mirror

for both, finally we get $120mm \ \langle \ f \ \langle \ 161mm$.

2.3.4. Beam Stop

If the central zero-order undiffracted beam hits the wall of the instrument housing,

there can be a small amount of stray photons that are reflected by the wall and directed to the

PMT. In order to avoid stray photons, a beam stop in the path of the undiffracted beam is placed.

The beam stop is simply a piece of thick paper painted with black paint.

2.4. Optimization

It is essential to deliberately locate each component involved in an optical system in relation to one another to achieve the optimal performance. The diffraction efficiency of an AOTF is largely dependent on the incidence angle as well as the selected wavelength and the RF signal power. The important feature of the NPM condition is that strong diffraction intensity may be maintained in the presence of poorly collimated incident light. However, poorly collimated light produces spectral broadening of the bandpass of the AOTF. The angle of incidence and collimation state of the incident light beam affect not only the bandpass and the central wavelength of the diffracted beams but also the state of background noise. One of the most challenging tasks in the arrangement of the optical components was to deal with this background light. The light that reaches the photosensitive area of the PMT cannot only be a narrowband of selection. It is inevitable to have a certain level of unwanted broadband background light propagating together with the diffracted light beams. The background noise consists mainly of out-of-band wavelength and is caused by high sideband levels, light diffracted by acoustic energy reflected at crystal surfaces, and light scattered by the crystal from its bulk, surfaces and coatings. Close to the main peak, high sidelobes are the principal cause of

the background, whereas further from the main peak phase matching to the divergent acoustic

wavevectors or to the reflected acoustic energy may be the dominant source [9]. The complex

behavior of background light was experimentally observed with a tungsten halogen lamp (LS-1,

Ocean Optics, Dunedin, FL) as a light source and the optimal orientations and positions of the

AOTF spectrometer components were searched based on SNR estimations. The following figure

denotes each dimension in the experimental setup.
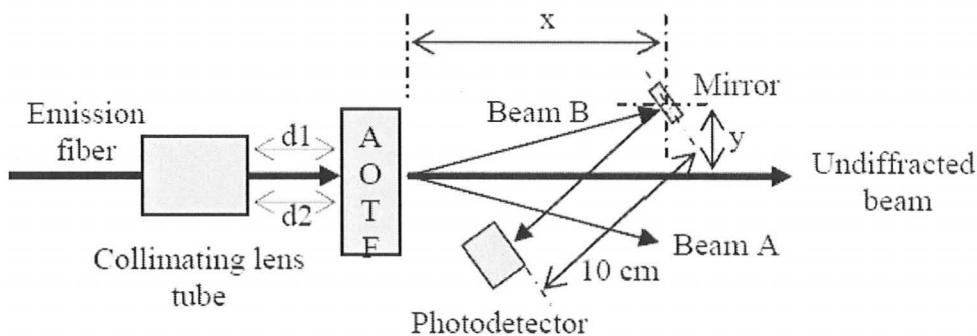
Fig. 2.16. Arrangement of the AOTF spectrometer components. The AOTF was rotated and the mirror was translated along x and y axes. The distance between mirror and photodetector was kept at 10 cm.

The distances d1 and d2 between the lens tube and the AOTF were changed by rotating

the AOTF, which varies the range of incident angle. The mirror was placed at a distance x from

the AOTF and a distance y from the undiffracted beam. The distance y was always set so as to

allow the center of the beam cross-section to hit the center of the mirror surface. An optical

power meter (1830, Newport, Irvine, CA) was used to detect the light reflected from the mirror

with its photodetector placed 10 cm away from the mirror. To investigate SNR of the AOTF set-

up, the AOTF was turned on and the wavelength of the diffracted beam was set at 510 nm. The

mirror was placed at distance x of 10, 20, and 23 cm from the AOTF. Light power of both

diffracted beams A and B was detected and combined. The level of background light was

measured with the AOTF turned off. The correction wavelength of the power meter was set at

510 nm to detect the diffracted beams when the AOTF was turned on and at 900 nm when the

AOTF was turned off. SNR was calculated using the equation below.

$$SNR = \frac{light\ power\ at\ 510nm_{AOTF-ON} - light\ power\ at\ 510\ nm_{AOTF-OFF}}{light\ power\ at\ 900nm_{AOTF-OFF}} \qquad \text{[Eq. 2.8.]}$$

The results are presented in the following graphs.
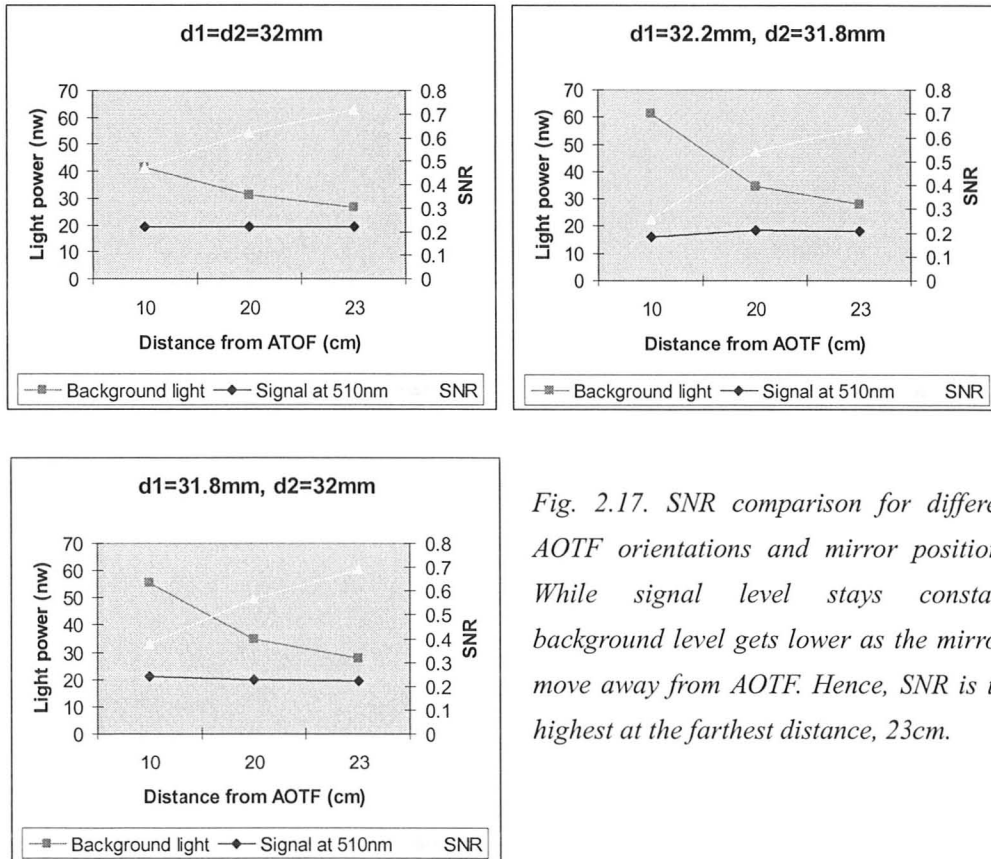
Fig. 2.17. SNR comparison for different AOTF orientations and mirror positions. While signal level stays constant, background level gets lower as the mirrors move away from AOTF. Hence, SNR is the highest at the farthest distance, 23cm.

It is noticed that the signal level is almost independent of the variation of mirror positions and the AOTF orientation whereas the intensity of background light is heavily dependent on such variations. It can be concluded that at 23 cm, the SNR is significantly better than at shorter distances because of the drastic decrease of background noise with increasing distance. Extending the distance farther than 23 cm was not considered due to the physical limits of instrumentation. As no significant difference in SNR is invoked by the change of AOTF orientation, the orientation $d1 = 31.8mm$ and $d2 = 32mm$ (slight counter-clockwise rotation) was chosen in consideration of the bandwidth of the combined diffracted beam.

The position of the beam stop is also worth an account to effectively increase the SNR. The beam stop was placed at 5 different distances (x in Figure 2.18.) from the AOTF. It was tilted with a certain angle to avoid potential direct reflection of undiffracted light to the PMT. In this observation, the PMT was used as a detector with a proper timing scheme and its output signal was amplified by a current preamplifier (SR570, Stanford Research Systems, Sunnyvale, CA) connected to the oscilloscope. The amplifier's gain mode was set to high bandwidth (High BW) and the sensitivity was set at 20 μA/V. The AOTF filtering wavelength was tuned to 350 nm to measure background noise because the light intensity from the tungsten halogen lamp at 350 nm is extremely low and negligible. For diffracted light, the filtering wavelength of the AOTF was set at 510 nm. The pulse data acquired by the oscilloscope were processed with

Matlab for integrating the intensity over the pulse duration time. The integrated intensity was

used to calculate the true signal at 510nm, SNR, SNR gain, signal loss using the following

definitions.

True signal at 510nm = raw signal at 510nm – background light (at 350nm)   *[Eq. 2.9.]*

$$SNR = \frac{true\ signal\ at\ 510nm}{background\ (at\ 350nm)}$$ *[Eq. 2.10.]*

$$SNR\ gain = \frac{SNR_{Beam\ stop\ at\ x} - SNR_{No\ beam\ stop}}{SNR_{No\ beam\ stop}}$$ *[Eq. 2.11.]*

$$Signal\ loss = \frac{true\ signal\ at\ 510nm_{No\ beam\ stop} - true\ signal\ at\ 510nm_{Beam\ stop\ at\ x}}{true\ signal\ at\ 510nm_{No\ beam\ stop}}$$ *[Eq. 2.12.]*
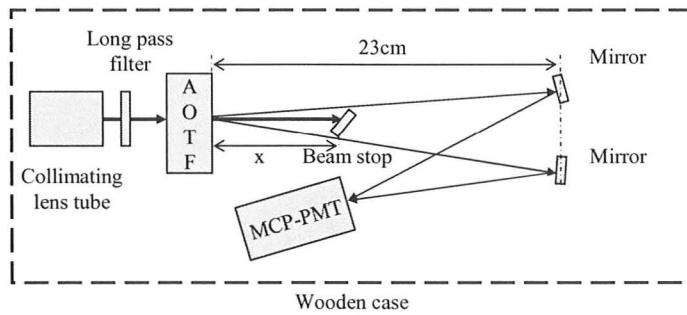
Fig. 2.18. Positioning the beam stop. Distance x was varied while signal, background and SNR variations were under observation.

Table. 2.1. SNR parameters for different positions of the beam stop

	Position of the beam stop, x (cm)					No beam stop
	5	8	10	12	15	
Background (350nm)	231.26	315.62	389.43	421.20	421.54	470.78
Raw signal at 510nm	339.89	459.72	545.16	572.32	574.97	628.86
True signal at 510nm	108.63	144.10	155.73	151.12	153.44	158.08
SNR	0.47	0.46	0.4	0.36	0.36	0.34
SNR gain (%)	38	35	18	6	6	
Signal loss (%)	31	8.8	1.5	4.4	2.9	
SNR gain / Signal loss	1.23	3.98	**12**	1.36	2.07	
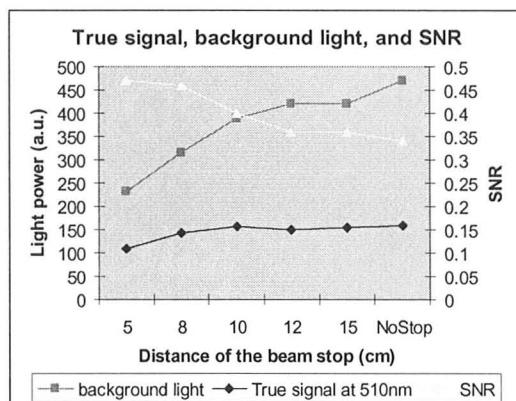
Fig. 2.19. True signal, background and SNR at different positions of beam stop.

The beam stop diminishes the signal level as well as background. As a compromise, the highest

ratio of SNR gain (Eq. 2.11.) and signal loss (Eq. 2.12.) was taken as the optimal condition.

Under this criterion, it was determined the beam stop has to be put 10 cm away from the AOTF.

References

1. L. Bei et al, *Acousto-optic tunable filters: fundamentals and applications as applied to chemical analysis techniques*, Progress in Quantum Electronics, **28**, 67-87 (2004).

2. P. N. Prasad, *Introduction to Biophotonics*, John Wiley & Sons (2003).

3. *Brimrose AOTF Manual*, Brimrose Corporation of America (2005).

4. I. C. Chang, Non-*collinear acousto-optic filter with large angular aperture*, Applied Physics Letters, **25** (7), 370-372 (1974).

5. G. Georgiev, D. A. Glenar, and J. J. Hillman, *Spectral characterization of acousto-optic filters used in imaging spectroscopy*, Applied Optics, **41**(1), 209-217 (2002).

6. J. Xu and R. Stroud, *Acousto-optic devices: principles, design, and applications*, Wiley

(1992).

7. G. Best and O. M. Sezerman, *Shedding light on hybrid optics: a tutorial in coupling*, Optics & Photonics News, Feb., 31-34 (1999).

8. F. L. Pedrotti, L. S. Pedrotti and L. M. Pedrotti, *Introduction to Optics*, 3rd ed., Pearson Prentice Hall (2007).

9. L. J. Denes, M. S. Gottlieb and B. Kaminsky, *Acousto-optic tunable filter in imaging applications*, Optical Engineering, **37**(4), 1262-1267 (1998).

3. System design

3.1. Overview of the system setup

The time-resolved fluorescence spectroscopy (TRFS) system consists of a pulsed Nd:YAG laser for UV excitation at 355 nm, a pulse generator, an acousto-optic tunable filter (AOTF), a time-gated microchannel plate photomultiplier tube (MCP-PMT), a digital oscilloscope and compatible optics. An image of the TRFS system housed in a mobile instrument cart is shown in Figure 3.1, while the block diagram of main components of the system is outlined in Figure 3.2.

Optical excitation pulses from the Nd:YAG laser are coupled by a lens into a bifurcated optical fiber probe to excite a target sample. The emitted fluorescence light from the excited sample is delivered by the collection channel of the probe to the non-collinear AOTF spectrometer unit. After passing through a longpass filter and a collimator, the emission pulses enter the AOTF crystal where acousto-optic diffraction takes place. The diffracted pulse beams are focused on the photosensitive area of the MCP-PMT by concave mirrors. The PMT converts the optical pulses to electrical signals, which is further amplified by an amplifier and digitized by the digital oscilloscope.

The data acquisition sequence is initiated by commanding the AOTF controller via a LabVIEW® interface to transmit an electrical pulse of 32 µs width for each wavelength to the

pulse generator and the corresponding radio frequency (RF) signals to the AOTF. For each

external trigger pulse from the AOTF controller, the pulse generator produces a train of 11

square wave pulses of 50 μs width in burst mode at 1 kHz, each of which is sent to the trigger

input of the laser. The pulse generator also sends 11 gating signals to the MCP-PMT. Each

external pulse to the laser produces a low jitter synchronization pulse from a built-in photodiode

and an optical laser pulse that is delivered to a fluorescent target through the fiber probe. A

channel on the digital oscilloscope receives amplified electrical pulses from the PMT and the

other channel is connected to the laser synchronization pulse output which serves as a waveform

record trigger reference. Time delay between the trigger pulses to the laser and the MCP-PMT

gating was introduced by the pulse generator to account for the delay of fluorescence emission

arriving at the MCP-PMT. A LabVIEW® program was developed to control every component to

achieve fully automated data acquisition process.
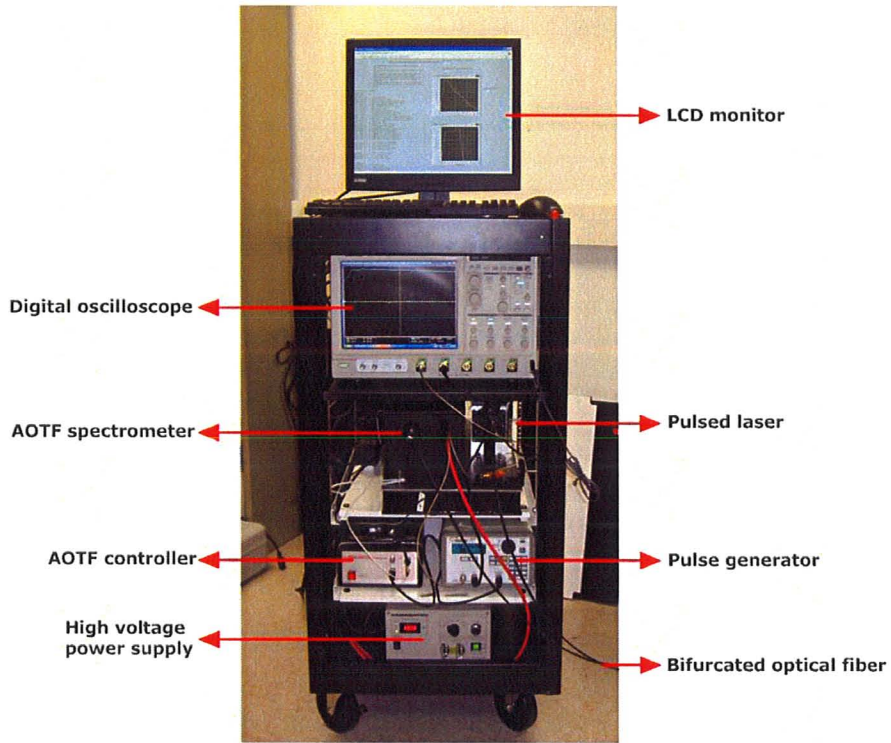
Fig. 3.1. tr-LIFS system in an instrument cart.
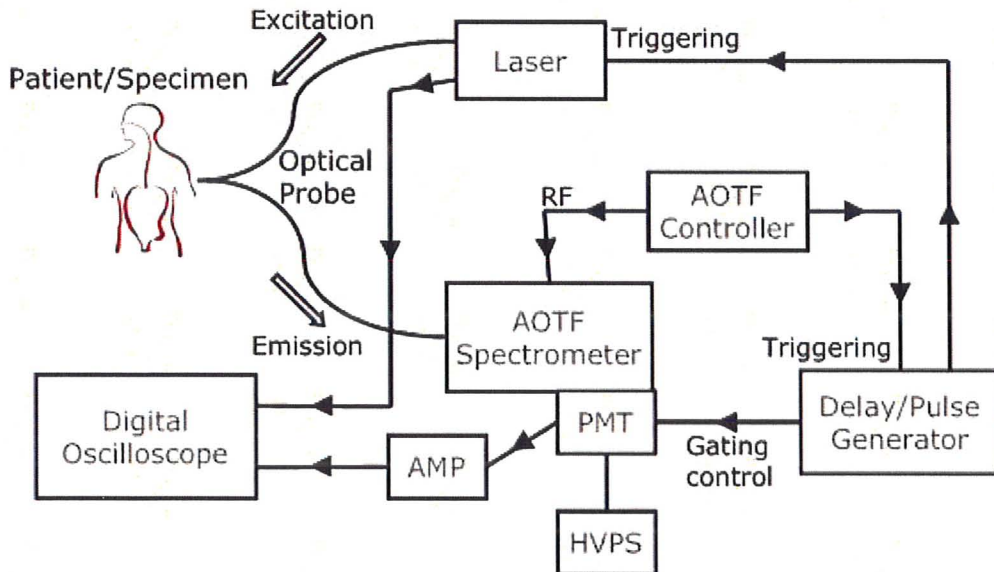
Fig. 3.2. Schematic of the tr-LIFS system setup. Signal flows are shown by arrows.

3.2. System Components

The excitation source chosen for this research is a frequency-tripled (from 1064 nm to

355 nm), passively Q-switched, diode-pumped solid-state Nd:YAG microchip laser (PowerChip

NanoLaser, PV-001525-140, Teem Photonics, Meylan, France, shown in Figure 3.3.). It operates

at a factory-optimized repetition rate of 1 kHz and has an output energy of about 22 μJ per pulse

with a full-width-at-half-maximum (FWHM) pulse duration of about 300 ps.
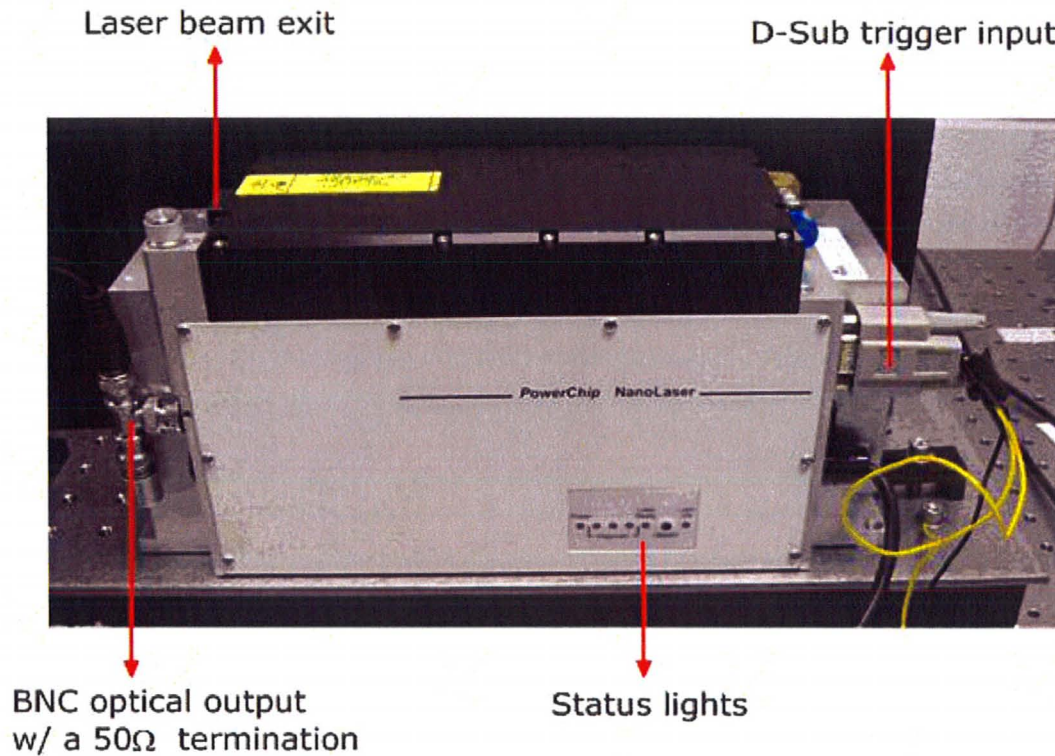
Fig. 3.3. Photograph of diode pumped Nd:YAG microchip laser.

While it is in the "Laser ON" mode, the laser is externally triggered through the D-Sub

female 9 pin input connected to the pulse generator. The diode laser current is activated by the

leading edge of an external trigger (Figure 3.4.). An optical pulse is then emitted by passive Q-

switching. As soon as the photo detector in the laser head detects the optical pulse coming out of

the microchip, it commands the electronic driver to turn off the diode current. Therefore, only

one optical pulse is permitted each time the oscillator leading edge is generated [1].
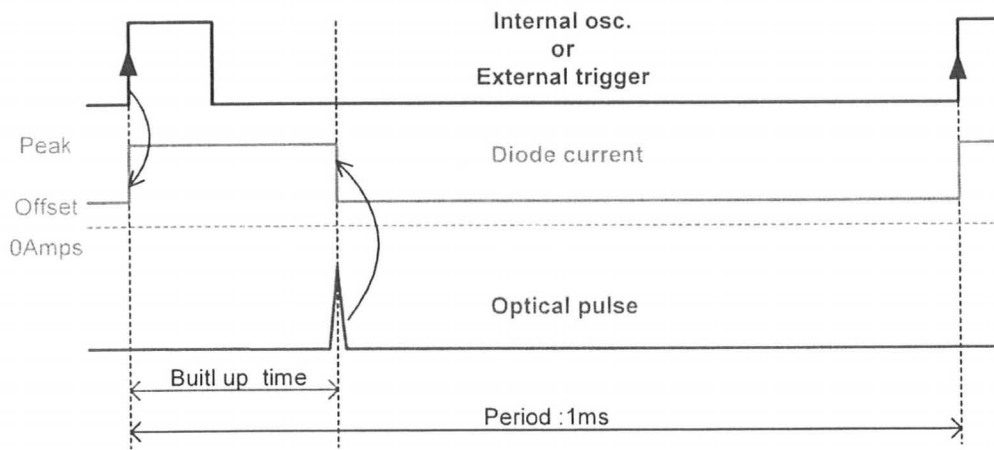
Fig. 3.4. Timing diagram of the diode laser operation. The diode current is activated by the leading edge of an external trigger. The photo detector in the laser head detects the optical pulse coming out of the microchip and commands the electronic driver to turn off the diode current [1].

The image of the optical pulse can be read in parallel through a BNC connector on the

front of the laser under the condition that the readout configuration is 50 Ohms terminated. The

following figures depict typical detector responses (waveform record trigger signals). The

detector rise time is approximately 10 ns.
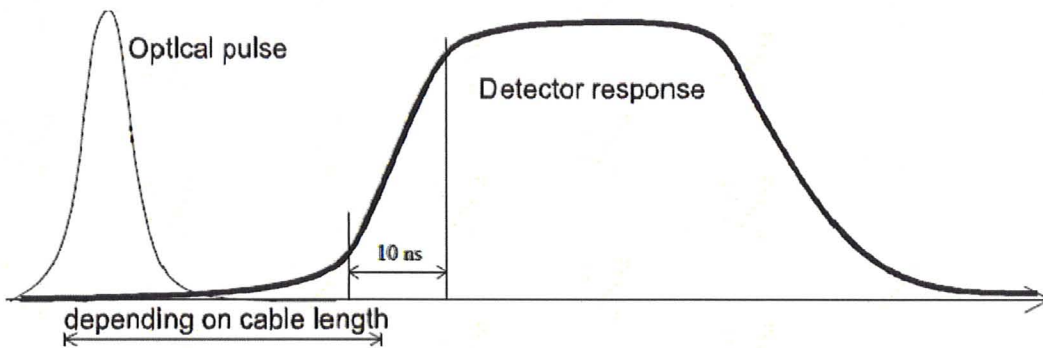
Fig. 3.5. Time relation between the laser output and the internal optical trigger output [1].
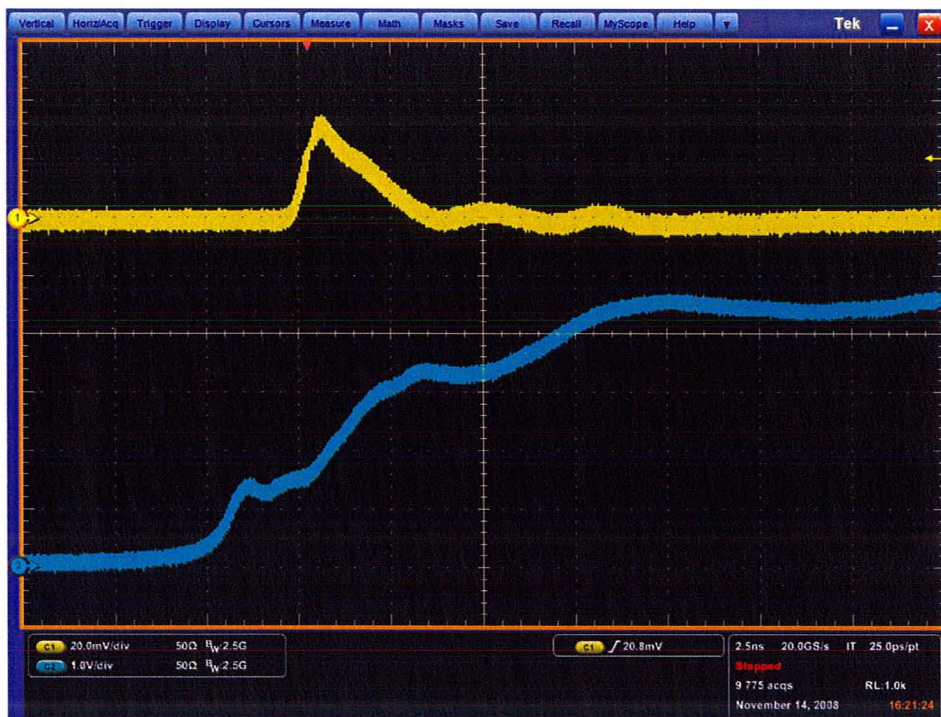
Fig. 3.6. Rising of the waveform record trigger signals recorded in 'Envelope' acquisition mode that finds the highest and lowest record points over many acquisitions (1k acquisitions in the figure) on the digital oscilloscope. The blue waveform is the trigger signal from the laser with about 10 ns rising time. Its wide plateaus on the rising edge can cause high jitter. As an alternative, an external Si-based photodetector (DET 10A, Thorlabs) was incorporated to detect reflected stray laser light outside the laser and trigger waveform acquisitions on the oscilloscope (yellow waveform).

As represented in the two figures below, a laser beam coupler is attached to the excitation fiber tip in front of the laser beam exit to prevent reflections of the laser in unwanted directions and deliver an adequate intensity of excitation light to the target through convenient adjustment. The focal length of the plano-convex lens used in the coupling system is 20 mm.
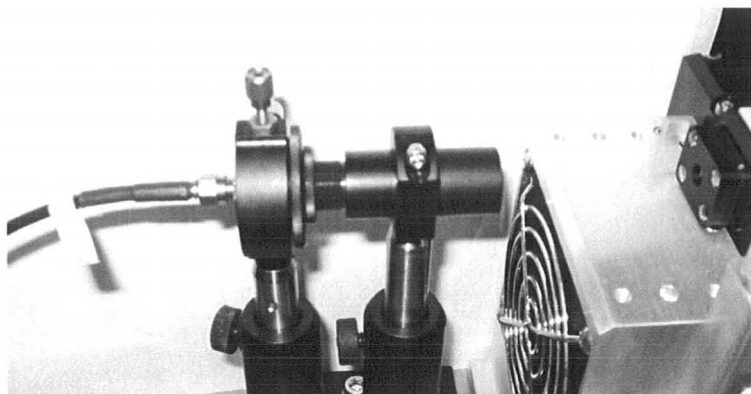
Fig. 3.7. Laser-fiber coupling. Excitation laser pulses are coupled into the excitation channel of the fiber probe in such a way that pulse energy at the distal end of probe is limited to 3 μJ.
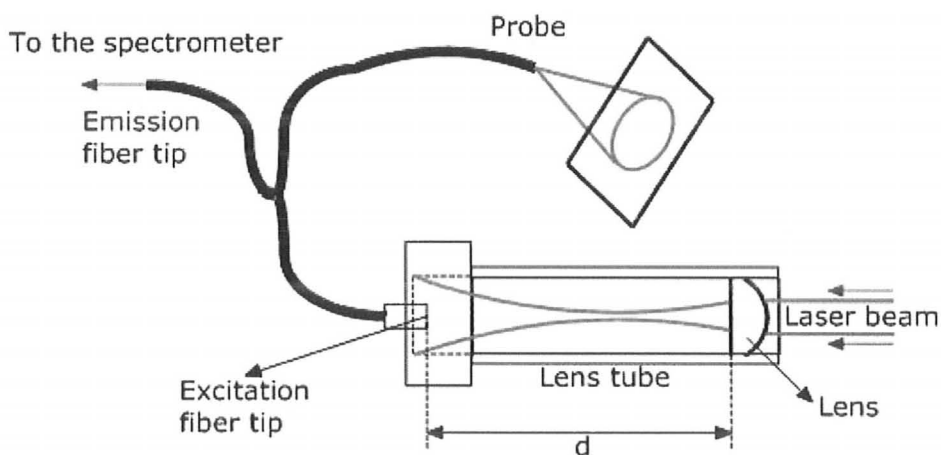
Fig. 3.8. Schematic of laser-fiber coupling.

The excitation light is coupled into a 600 μm diameter 0.12NA optical fiber and is delivered to a target. The intensity of excitation light coming out of the distal end of the probe

must be limited to about 3 μJ in order not to damage biological samples [2]. According to the

measurements (Figure 3.9.), 6 cm between the fiber-end and the flat side of the selected lens

was found to be suitable to satisfy the condition.
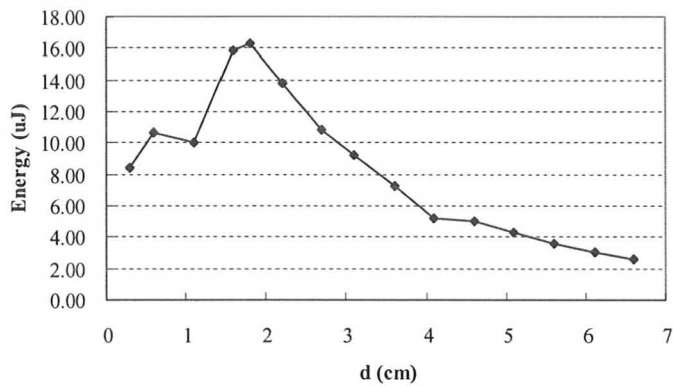
Fig. 3.9. Excitation pulse energy as a function of the distance between fiber probe input and coupling lens (d in Fig. 3.8.). The excitation pulse energy was measured by a laser power/energy meter (3 Sigma, Coherent, Santa Clara, CA) optimized for 355 nm incident light at the distal end of the excitation fiber probe tip.

A spatial intensity profile of excitation light was observed by imaging the paper

fluorescence induced by the excitation channel of the fiber probe (Figure 3.10.). It was noted

that the output intensity profile is affected by curvatures of the optical fiber. This occurrence is

prominent in a multimode step-index fiber where two adjacent modes are not evenly spaced. An

introduction of a mode scrambler may lead to a wide spectrum of spatial frequencies and thus

provide a more uniform spatial mode distribution that is independent of the excitation condition

and physical irregularities of the fiber [3].
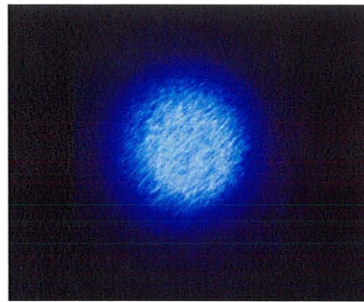
Fig. 3.10. Image of paper fluorescence excited by Nd:YAG laser from the fiber probe. This cross-section profile is subject to the curvatures of the delivery fiber.
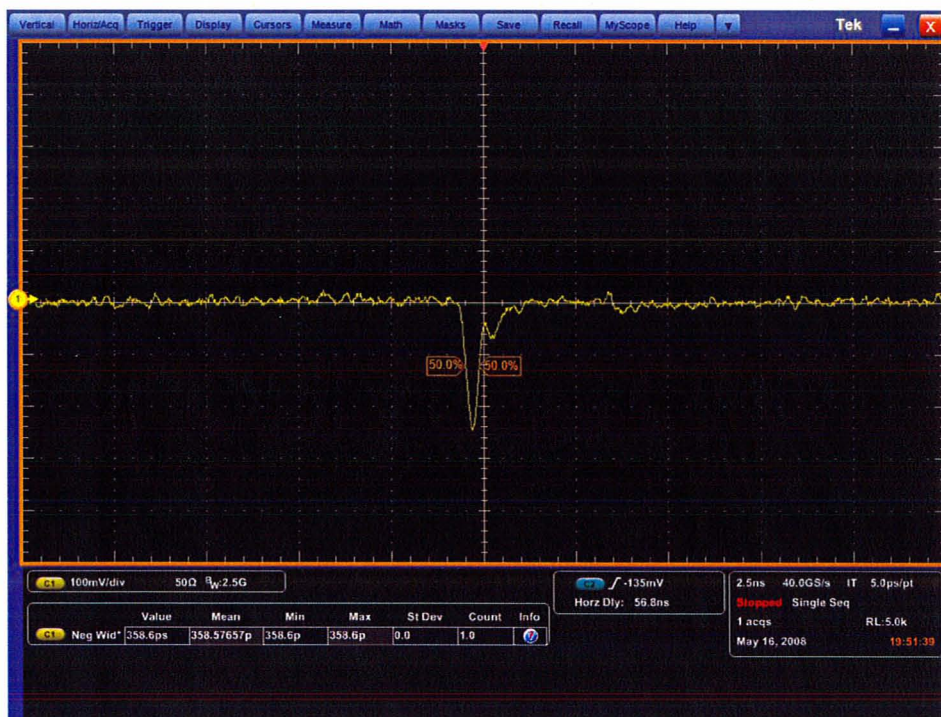
Fig. 3.11. Back reflection of laser occurring inside the lens tube causes additional peaks on the emission waveform. Temporal delay of 0.4 ns between the first and second peaks approximately corresponds to 12 cm path for a round trip of photons.

A customized bifurcated fiber optic probe with SMA connections (CeramOptec, P/N 50-2632-REV1, non-solarizing silica/silica step index optical fibers of 0.12 NA +/- 0.02 suitable for transmission wavelengths from 193 nm to 1200 nm) was used. The probe bundle assembly

consists of one central piece of 600 µm core diameter fiber for delivering excitation light and 12

fibers of 200 µm core diameter that surround the excitation fiber in order to collect emission.

Cores, claddings and coatings were made from pure fused silica, doped silica and polymide,

respectively [4]. The detailed configuration of the probe is shown in the following figures.
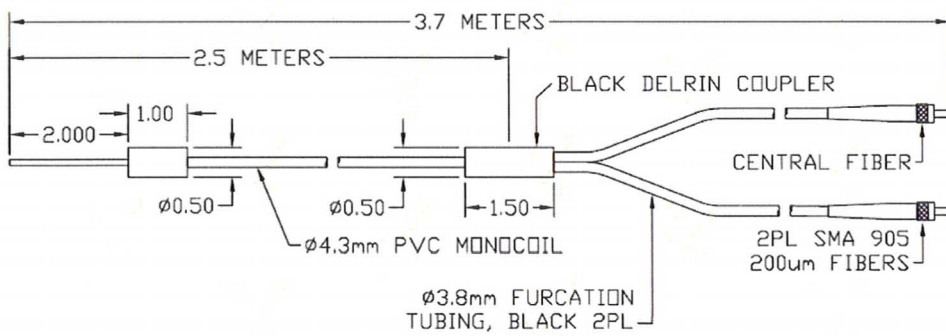
Fig. 3.12. Bifurcated optical fiber probe [4].
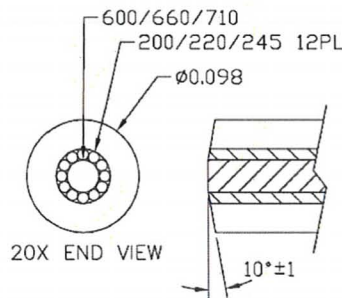
Fig. 3.13. Distal end of the fiber probe [4].
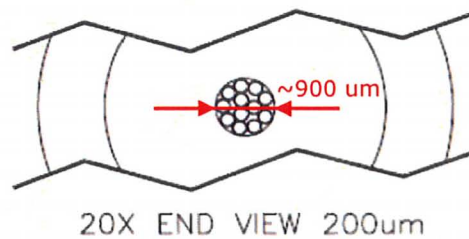
Fig. 3.14. Cross-section of the emission fiber bundle [4].

In a non-collinear AOTF, the first-order diffraction beams are separated from the undiffracted (zero-order) beam by diffraction. The undiffracted beam exits the AOTF at the same angle as the incident light beam whereas the narrowband diffracted beams with selected central wavelengths exit the device at a small angle with respect to the incident beam. In this study, we have designed a non-collinear AOTF spectrometer that collects both first order diffracted beams instead of only one to maintain the overall throughput high enough. The course of each light propagation is demonstrated in Figure 3.16. Emission light from the optical fiber is collimated by a plano-convex lens and delivered to the AOTF after going through a longpass filter. The AOTF transmits two beams of 1st order diffraction light and a central undiffracted beam. The two diffracted beams travel to the photosensitive area of the MCP-PMT after being reflected off by the concave mirrors while the undiffracted beam is blocked by a beam stop. The PMT multiplies the electrical signal produced by incident light. The electrical signal is then sent to the preamplifier and digitized by the digital oscilloscope. As elaborated in the previous chapter, this unit is of great importance determining the performance of the system.
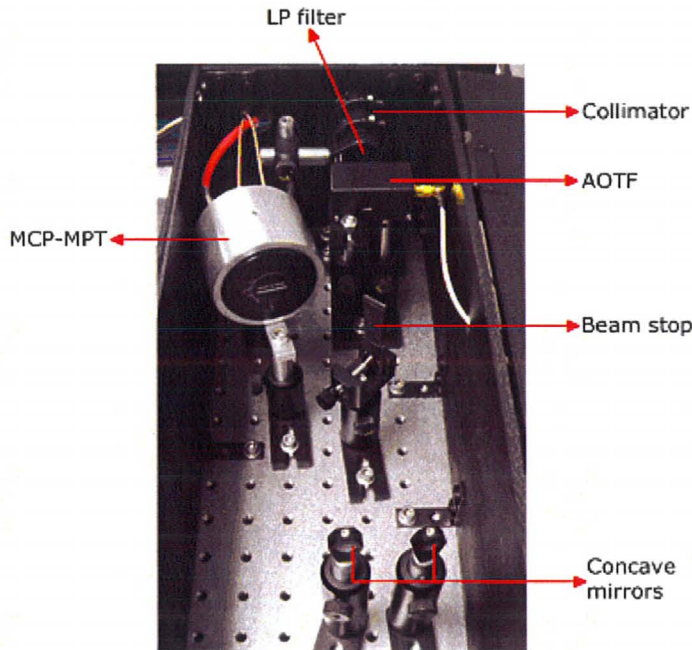
Fig. 3.15. AOFT spectrometer setup. The housing dimensions are 21 in × 7 in × 6.5 in.
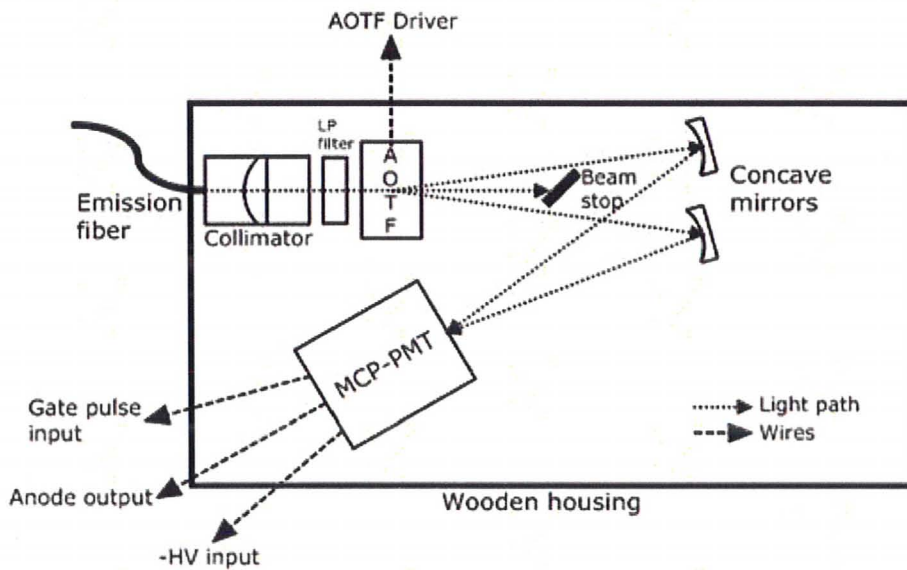
Fig. 3.16. Schematic of the AOFT spectrometer unit.

The most critical component for timing in the system may be the detector that converts

incident light to electrical signals. Photomultiplier tubes (PMTs) are considered the best detector

for almost all fluorometers. PMTs are extremely sensitive detectors of light in a wide

wavelength range, which respond to individual photons. The combination of high frequency

response, large photosensitive area, high gain and low noise has earned PMTs an essential place

in many fields of science. Especially, the microchannel plate photomultiplier tube (MCP-PMT)

has been the detector of choice for tr-LIFS systems. A MCP-PMT has narrow channels lined

with dynode material along which photoelectrons are amplified. Such channels let electrons

travel the same path, resulting in less transit time spread that limits the time resolution of the

PMT. MCP-PMTs can provide tenfold shorter pulse width than other types of PMTs and display

lower intensity afterpulses. The effects of wavelength and spatial location of incident light tend

to be much smaller with MCP-PMTs than with linear-focused or side-window PMTs. MCP-

PMTs also show high speed performance and the absence of timing artifacts. However,

disadvantages of MCP-PMTs include relatively small ranges of incident intensities that ensure

linear behavior, limited useful lifetime and high costs [5].
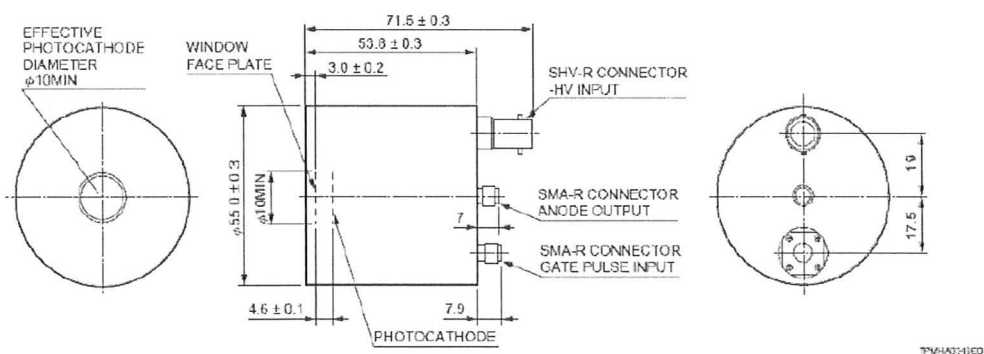
Fig. 3.17. R5916U-50 MCP-PMT (unit: mm) [6]

A gated MCP-PMT (R5916U-50, 2GHz, Hamamatsu Photonics, Japan) was used as

the photon detector for our system. According to the specification sheet provided by the

manufacturer, the output waveform rise time defined as the mean time difference from 10 to 90%

of peak amplitude was 184 ps and the gate rise time was 1 ns, which is insignificant compared

to the microsecond scale gate width. The acceptable gate width is between 5 ns and 10 μs with

maximum duty cycle of 1%. The working spectral response range is limited from 160 to 850 nm

while peaking at 430 nm as shown in Fig. 3.18. The photocathode effective area is 10 mm in

diameter [6].
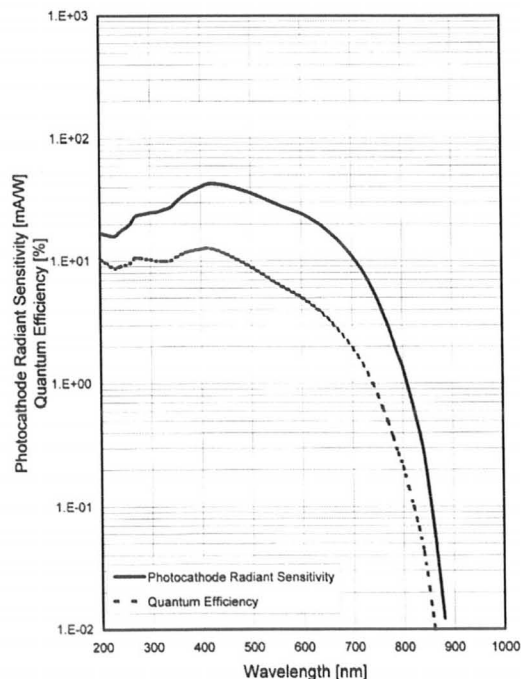
Fig. 3.18. Spectral response characteristics of the PMT [6]

The photocathode of the PMT should be held at a high negative potential. This is

achieved by a high voltage power supply (C4840-01, Hamamatsu Photonics, Japan), which

provides adjustable output from 0 to 3 kV. A SHV-SHV high voltage power cable is used to

connect the PMT high voltage input (SHV male) to the high voltage power supply output (SHV

male).

The pulse/delay generator (9512, Quantum Composers, Bozeman, MT) plays a key

role in synchronization. It can be externally triggered and operated in burst mode as well as

single shot, continuous and duty cycle mode with very low electronic jitter (< 400ps).
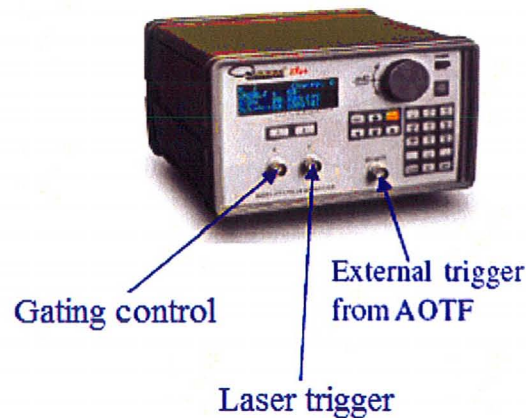
Fig. 3.19. 9512 Digital Delay/Pulse Generator and its specifications [7].

A digital oscilloscope (DPO7254, Tektronix, Beaverton, OR) initiates data collection

and processes every incoming data with the user interface. The digitizer has a very high

sampling rate (40 GHz for single channel) and analog bandwidth (2.5GHz). It can be operated

in Fast Frame mode that enables the digitizer to fetch and temporarily save a sequence of frames

in the internal memory. An external host computer is not required as Windows XP operating

system is embedded in the oscilloscope, reducing the physical size of our system and data

acquisition time.
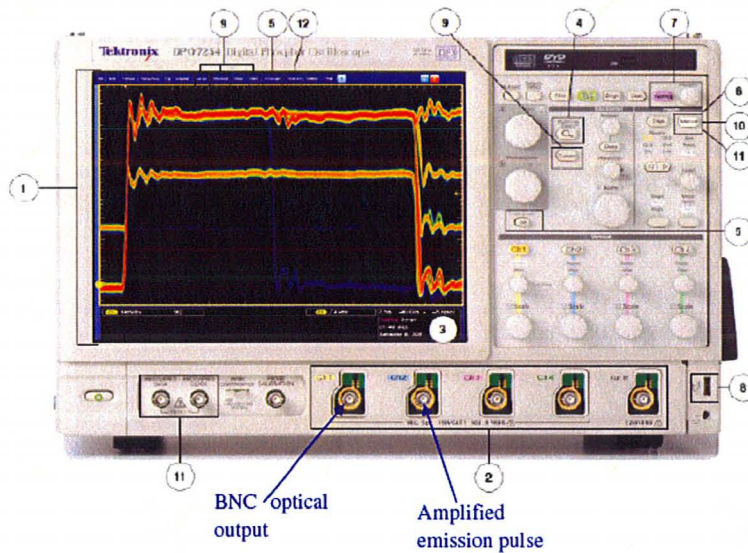
Fig. 3.20. DPO 7254 Digital Phosphor Oscilloscope [8]

The electrical pulses from the PMT are amplified by a high speed amplifier (C5594, Hamamatsu Photonics, Japan). The amplifier has wide frequency bandwidth from 50 kHz to 1.5 GHz. It also has very high gain as 36 dB so that it amplifies enough even for very weak PMT output signal [9]. 15V DC is supplied to it.
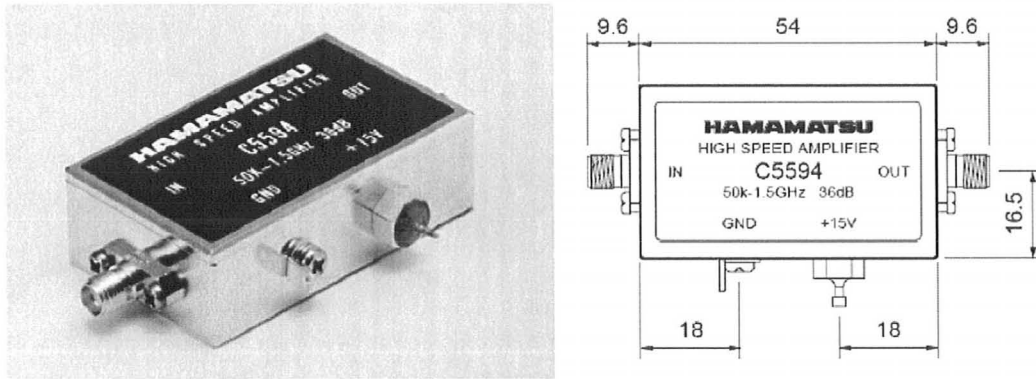
Fig. 3.21. High speed amplifier [9]

An uninterruptible power supply (UPS: APC Back-UPS XS 1500VA, American Power Conversion, West Kingston, RI) is used to provide instant protection in the event of momentary power interruptions to prevent loss of data. The maximum configurable power is 865 W and its typical recharge time is 6 hours. It is estimated based on Table 3.1. that if there is a blackout in the building, the UPS in our system will continue to provide sufficient power for the entire system to run for about 12 minutes at about half load [10].

Table 3.1. Power consumption estimation of each component

Device	Power consumption (W)	% Max. load
Oscilloscope + LCD monitor	343	39
Laser w/ driver	56	6
Pulse generator	13	1
AOTF w/ driver	24	2
PMT w/ HVPS	24	2
Pre-amplifier	4	0
The whole system running	475	55

3.3. System synchronization

The importance of precise timing control must be emphasized in order to accurately retrieve the nano- or pico-second time scale of fluorescence lifetimes. The factors that mainly affect the system timing are the optical/electronic delays, jitter and the PMT gate width controlling scheme. The purpose of the system synchronization is to trigger the laser, the PMT gate and the Fast Frame acquisition mode of the digital oscilloscope while ensuring every fluorescence pulse falls within the effective region of the PMT gate and the jitter between the pulses is minimized to avoid signal distortions.

An external pulse from the AOTF controller triggers the QC9512 pulse generator to produce two synchronized trains of 11 pulses at 1 kHz (1 ms per pulse) in burst mode (refer to Figure 3.2.). The delay setting on the pulse generator between the two output pulse trains has to accommodate the optical and electronic delays in such a way that the gate opening of the PMT and the arrival of fluorescence emission photons at the PMT can happen at the same time. It was experimentally determined that the trigger of the PMT gating electronics (20V, 6 μs wide) must be transmitted 128 μs later than the laser trigger (4V, 50 μs wide) [11]. It was also found that the time interval between external pulses from the AOTF controller must be set to above 8 ms (the actual measured interval is longer) to avoid signal distortions. The interval can be adjusted on the LabVIEW user interface and will be normally set to a larger value (50 ms) than the

minimum.

To determine the PMT gate width to allow every emission pulse to fall within the effective region of the open gate, the level of jitter has to be observed. The most dominant source of jitter is the Nd:YAG laser due to the uncertainties involved in the operational mechanism of cavity. The gate width of 6 μs was found to be wide enough to allow every pulse to be captured completely.

The waveform acquisition on the digitizer is triggered by the BNC optical output from the laser instead of the signal from the PMT, which cannot be regarded as a reliable trigger reference as its amplitude depends on the wavelength of incident light and can become as low as noise level. The low jitter (<50 ps) optical output synchronized with excitation pulses, on the other hand, has constant amplitude (~200 mV) independent of incident photons and can provide a stable trigger level for data acquisition.

The data acquisition process is automated by a LabVIEW (ver. 8.20, National Instruments, Austin, TX) program that can control all main system components via various communication protocols such as serial (RS-232), general purpose interface bus (GPIB) and local area network (LAN) interfaces. System synchronization and programming was covered in more detail in Yuan Zhang's thesis [11].

References

1. *Principles of Operation for PowerChip NanoLasers*, Teem Photonics (2006).

2. Q. Fang, T. Papaioannou, J. A. Jo, R. Vaitha and K. Shastry, *Time-domain Laser-induced Fluorescence Spectroscopy Apparatus for Clinical Diagnostics*, Review of Scientific Instruments, **75**(1), 152-162 (2004).

3. A. G. Hallam, D. A. Robinson and I. Bennion, *Mode Control for Emerging Link Performance Standards*, IET Optoelectronics Jornal.

4. *50-2632-REV1 data sheet*, CeramOptec.

5. J. R. Lakowicz, *Principles of Fluorescence Spectroscopy*, 3rd ed., Springer (2006).

6. *R5916U-50 Series data sheet*, Hamamatsu Photonics.

7. *9500 Series Pulse Generator Operating Manual*, Quantum Composers (2006)

8. *DPO7000 Series and DSA/DPO70000 Series Digital Phosphor Oscilloscopes Quick Start User Manual*, Tektronix.

9. *C5594 Manual*, Hamamatsu Photonics.

10. Back-UPS XS 1500 Specifications on the American Power Conversion website: http://www.apcc.com/resource/include/techspec_index.cfm?base_sku=BX1500.

11. Y. Zhang, *Time-domain Fluorescence Spectroscopy*, Master's Thesis, McMaster University (2007).

4. System Characterization

4. 1. Spectral response and wavelength calibration

The TeO$_2$ AOTF in this study is optimized for extraordinarily polarized input light (ordinarily polarized output). This means the spectral resolution for the o-beam is optimized and the o-beam has narrower spectral bandpass than the e-beam. Also, slightly different wavelength ranges for the two input polarization states are generated by the same acoustic frequency since the RF-wavelength relations for the first orders are a little shifted with respect to each other. The general non-collinear RF-wavelength tuning relations can be given by the following equations [1]. The acoustic frequency for the o- and e-output ($f_{o'}$ and $f_{e'}$) can be described as

$$f_{o'} = \frac{V}{\lambda} n_e(\theta_i) \left[\cos(\theta_i - \theta_a) + \left\{ \cos^2(\theta_i - \theta_a) + \left[\left(\frac{n_o}{n_e} \right)^2 - 1 \right] \sin^2 \theta_i \right\}^{1/2} \right] \quad [Eq.\ 4.1.]$$

$$f_{e'} = \frac{V}{\lambda} n_e(\theta_a) \left[C(\theta_i) + \left\{ C(\theta_i)^2 - \left[\left(\frac{n_o}{n_e} \right)^2 - 1 \right] \sin^2 \theta_i \right\}^{1/2} \right] \quad [Eq.\ 4.2.]$$

where θ_i = incident angle, θ_a = acoustic walk-off angle,

n_e = refractive index for e-light, n_e = refractive index for o-light,

λ = wavelength,

$$C(\theta_i) = \frac{n_e(\theta_a)}{n_o} \left[\cos\theta_a \cos\theta_i + \left(\frac{n_o}{n_e} \right)^2 \sin\theta_a \sin\theta_i \right]$$

$$V = \left(\frac{\frac{C_{11} - C_{12}}{2} \cos^2 \alpha + C_{44} \sin^2 \alpha}{\rho} \right)^{1/2} = \text{velocity of acoustic wave in TeO}_2,$$

$\alpha = 90° - \theta_a$ = acoustic tilt angle,

C_{11}, C_{12}, C_{44} = elastic constants of TeO$_2$,

ρ = density of TeO$_2$.

The fact that indices of refraction are, in fact, functions of the wavelength adds more complexity. The refractive index fit equations for TeO$_2$ are as follows [1]. λ is in μm and the applied best-fit Sellmeier coefficients are valid from 400 nm to 3.5 μm.

$$n_e{}^2 = 1 + \frac{4.33449\lambda^2}{\lambda^2 - 0.20242^2} + \frac{0.14739\lambda^2}{\lambda^2 - 4.93667^2} \qquad [Eq.\ 4.3.]$$

$$n_o{}^2 = 1 + \frac{3.71789\lambda^2}{\lambda^2 - 0.19619^2} + \frac{0.07544\lambda^2}{\lambda^2 - 4.61196^2} \qquad [Eq.\ 4.4.]$$

It should be noted that while the refractive indices vary with the wavelength, the difference between them $(\Delta n = n_e - n_o)$ does not change significantly. For simplicity, we can also consider the following approximated tuning relation that puts emphasis on the major variables [2]. When the other variables are held constant, the tuned wavelength is inversely proportional to the applied acoustic frequency.

$$\lambda = \frac{V\Delta n\sqrt{\sin^4\theta_i + \sin^2\theta_i}}{f} \qquad [Eq.\ 4.5.]$$
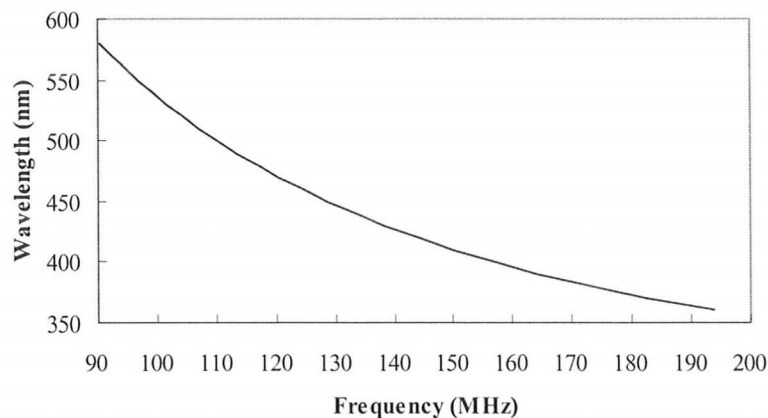
Fig. 4.1. AOTF wavelength tuning relation displayed by SPFII after wavelength calibration.

With the aforementioned knowledge, wavelength calibration of the system was performed using a standard mercury argon calibration lamp (HG-1, Ocean Optics, Dunedin, FL) and an optical spectrometer (OSM-400 UV/VIS, Newport, Irvine, CA). The accuracy of the optical spectrometer was tested with the standard lamp. A 1 m long, 400 μm diameter core fused silica optical fiber was connected to the spectrometer and its tip was used as a probe. The wavelengths of mercury spectral lines detected by the spectrometer were in good agreements (less than 0.5 nm discrepancies) with the given spectrum of the lamp.

The accuracy of the AOTF's wavelength tuning was verified by measuring the selected wavelength of the diffracted beams using the fiber optic spectrometer. A halogen lamp with continuous visible spectrum was used as an input source. When one wavelength (460 nm) was selected on the AOTF control panel (SPFII software), the narrow bandpass spectra of the two resulting first order diffraction beams were measured by the optical spectrometer from 360 nm to 570 nm at 10 nm increments as shown in Table 4.1. It has been found that over the spectral range of interest, discrepancies from the wavelengths selected on the AOTF control panel were less than 2.5 nm, which is acceptable considering the spectral resolution of the system.

Table 4.1. Comparison between selected wavelengths on SPFII
and measured AOTF output peak wavelengths

AOTF	e-beam		o-beam	
Wavelength (nm)	Wavelength (nm)	Intensity (a.u.)	Wavelength (nm)	Intensity (a.u.)
380	379.6	0.388	379.3	0.060
390	389.3	1.165	389.6	0.160
400	399.4	1.854	399.4	0.291
410	409.4	2.586	409.7	0.450
420	419.7	2.819	420.0	0.577
430	429.7	3.362	430.0	0.839
440	440.4	3.046	440.7	0.834
450	450.4	2.553	449.8	1.124
460	459.3	4.983	460.2	1.757
470	469.4	7.135	470.0	2.677
480	479.4	8.513	480.0	3.287
490	489.5	14.180	490.1	5.217
500	499.6	19.270	500.2	6.594
510	509.6	20.110	510.2	6.766
520	519.7	18.440	520.6	6.101
530	529.5	15.600	530.4	5.686
540	539.5	12.980	540.4	5.086
550	549.3	10.510	550.2	4.152
560	559.4	8.229	560.3	3.676
570	569.2	5.689	570.4	2.633
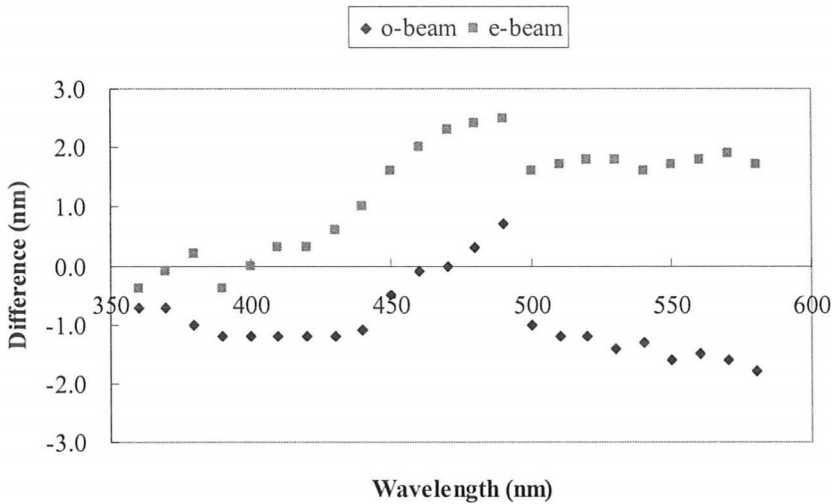
Fig. 4.2. Discrepancies of peak wavelengths of AOTF diffraction beams
measured by OSM-400 from selected wavelengths on SPFII.

It was also noticed that peak intensity of the ordinary beam was up to about 4 times higher than that of the extraordinary beam with this setup of the AOTF. This disparity in throughput was empirically unavoidable in order to keep the differences between the peak wavelengths of both beams minimal. The AOTF diffraction efficiency is strongly influenced by the wavelength and the angle of incidence. The spectral dependence of the diffraction efficiency has an oscillating character forming successive regions of high and low levels, which can be heavily affected by the incident angle. With increasing incident angle, the spectral regions of high diffraction efficiency slightly broaden whereas they significantly decrease in magnitude and shift to shorter wavelengths. Also, the photon-phonon interaction length within the birefringent crystal is one of the elements governing the diffraction efficiency. A minor increase of the interaction length can lead to remarkable broadening of the spectral bands of high diffraction and their shift towards longer wavelengths [3]. The overall interaction length difference for e- and o- light due to the AOTF orientation and crystal geometry may be one of the causes of this phenomenon highlighted in Fig 4.3.
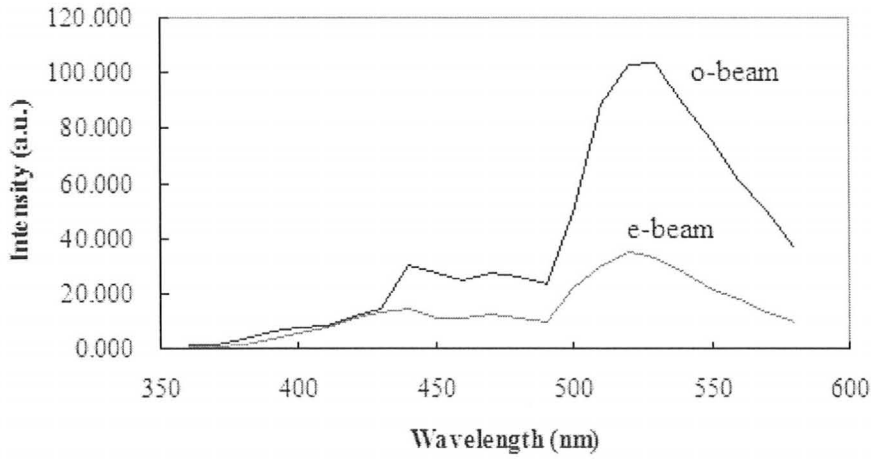
Fig. 4.3. Peak intensity spectra of AOTF diffraction beams measured by OSM-400.
Each diffraction beam was focused by a lens onto the tip of the optical spectrometer's fiber
probe and its relative intensity at various wavelengths was measured. Intensity of ordinary beam
appeared higher than extraordinary beam throughout the entire spectral range.

The bandpass shape of a non-collinear AOTF is ideally a sinc^2(x) function and the full

width at half maximum (FWHM) bandpass of the central lobe can be approximated by the

equation [1]

$$\Delta\lambda = \frac{1.8\pi\lambda^2}{B(\lambda)L\sin^2\theta_i} \qquad\qquad [Eq.\ 4.6.]$$

where $\quad L = \dfrac{W}{\cos(\theta_i - \alpha)}$ = acousto-optic interaction length

W = transducer width

$B(\lambda) = 2\pi\left(\delta n - \lambda\dfrac{\partial\delta n}{\partial\lambda}\right)$ = optical dispersive constant

$\delta n = n_e - n_o$

If $\dfrac{\partial\delta n}{\partial\lambda}$ is assumed to be negligible, the equation can be simplified as

$$\Delta\lambda = \frac{0.9\lambda^2}{\Delta n L \sin^2\theta_i} \qquad\qquad [Eq.\ 4.7.]$$

In this approximation, the bandpass is proportional to the square of the wavelength and

inversely proportional to the interaction length. The FWHM bandpass from 380 to 570 nm

measured by the OSM spectrometer ranged from about 2 to 3 nm. The bandpass at 406 nm was

also measured by using the complete data acquisition process of the system through scanning a

pulsed diode laser (LDH-405, PicoQuant, Berlin, Germany) with its peak emission at 406 nm.

The communication scheme is presented in Figure 4.4. The FWHM bandpass of the time-

integrated spectrum of the laser was about 3 nm (Figure 4.5.).
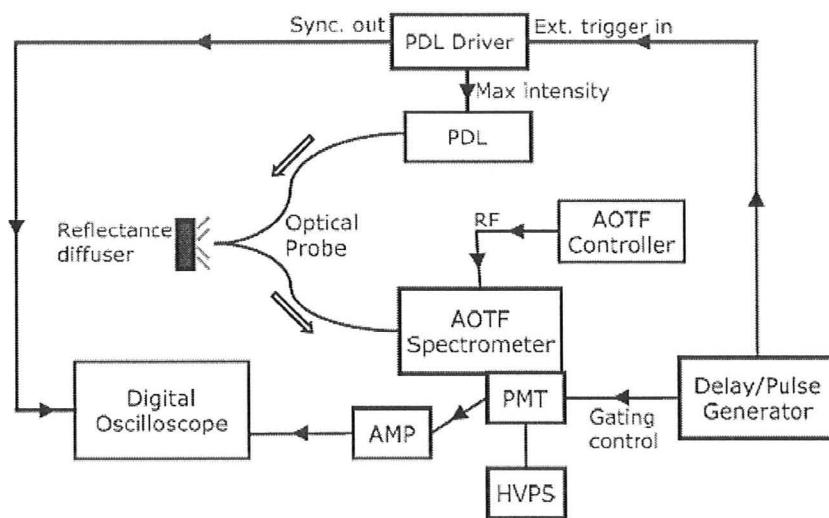
Fig. 4.4. Schematic of pulsed diode laser (PDL) scanning. The Nd:YAG laser in the original system setup was replaced with the diode laser (40 MHz) and the time settings were adjusted accordingly.
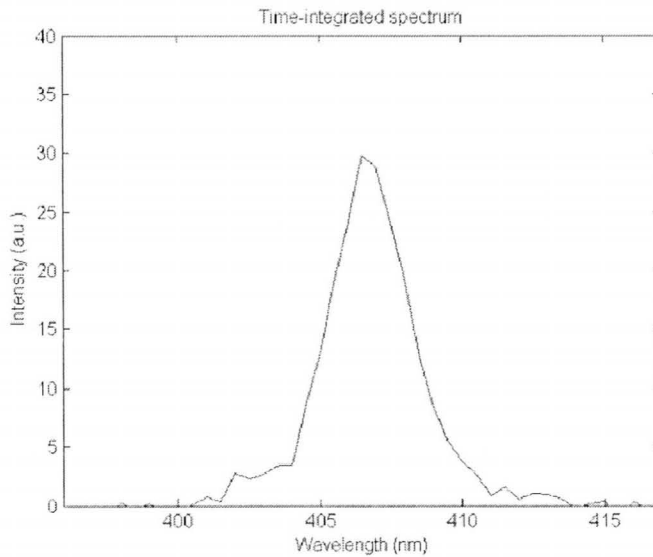
Fig. 4.5. Time-integrated spectrum of the 406 nm pulsed diode laser. 30 pulses were recorded and averaged for each wavelength with 0.5 nm increment. The FWHM is about 3 nm.

4. 2. Spectral intensity calibration

The diffraction efficiency of the AOTF and the responsivity of the MCP-PMT (Fig. 3.18.) are dependent on incident wavelength. This spectral dependence of the main components of the system calls the need for spectral intensity calibration in order to accurately present any measurements by the system. The goal is to obtain the system's measured intensity correction factor as a function of wavelength in the working range. Any measured emission spectrum may be corrected by dividing it with the spectral correction function.

A calibrated tungsten halogen lamp (HL-2000-CAL, Ocean Optics) was used as a broadband standard calibration light source. Because the calibration light source's output was too low to work properly in the scheme, a non-calibrated lamp (LS-1 tungsten halogen light source, Ocean Optics) with much higher output was employed as a primary light source. The

spectra of both light sources were measured using the OSM optical spectrometer. The relative

intensity values measured by the spectrometer cannot be taken as they appear since the device's

sensitivity also has spectral dependence (Figure. 4.6.).
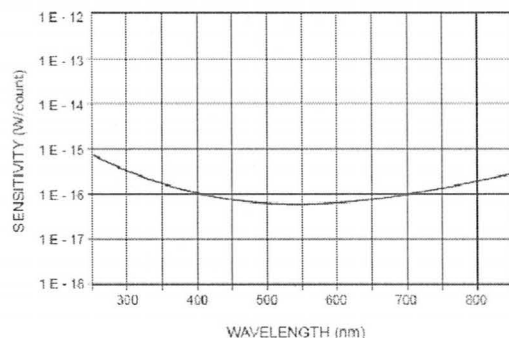
Fig. 4.6. Sensitivity curve for OSM-400 UV/VIS spectrometer from the user manual [4]

The first stepping stone that can be trusted is the spectral data of the calibration light source

given by the manufacturer. Table 4.2. lists every necessary information to acquire the spectral

correction function of the system. The spectral intensity of HL-2000 measured by the OSM

spectrometer (M) at each wavelength is divided by the given value (G). The resulting factors (C)

are then regarded as a sensitivity function of the spectrometer and used to correct the spectral

intensity of LS-1 measured by the spectrometer (I). Finally, the corrected intensity (R) is

compared to the spectral intensity of LS-1 measured by the tr-LIFS system (E) to produce the

correction (sensitivity) factors for the system. The resulting correction function is shown in

Figure 4.7.

Table. 4.2. Spectral correction factors

Wavelength (nm)	Intensity (a.u.)						
	Spectrometer					System	
	HL-2000 (Calibration source)			LS-1		LS-1	
	measured	given	correction factors	measured	corrected	measured	correction factors
	M	G	C=M/G	I	R=I/C	E	S=E/R
360	0.120	4.094	0.02931	3.82	130.25	0.34	0.002610
370	0.146	5.815	0.02514	4.70	187.09	2.4933	0.013327
380	0.157	7.275	0.02160	5.27	243.98	7.8253	0.032074
390	0.201	10.274	0.01958	6.51	332.55	19.3975	0.058330
400	0.245	13.073	0.01872	7.72	412.60	34.6823	0.084058
420	0.392	20.940	0.01870	11.79	630.73	80.545	0.127701
440	0.609	32.455	0.01875	17.23	918.96	139.4502	0.151748
460	0.883	47.044	0.01878	23.84	1269.43	163.467	0.128772
480	1.300	66.255	0.01963	33.07	1685.16	222.8573	0.132247
500	1.817	90.401	0.02010	43.56	2166.84	182.8018	0.084363
525	2.730	131.250	0.02080	62.25	2992.42	102.5894	0.034283
550	3.749	178.450	0.02101	80.68	3840.66	55.7498	0.014516
575	5.189	234.340	0.02214	106.17	4794.28	28.5847	0.005962
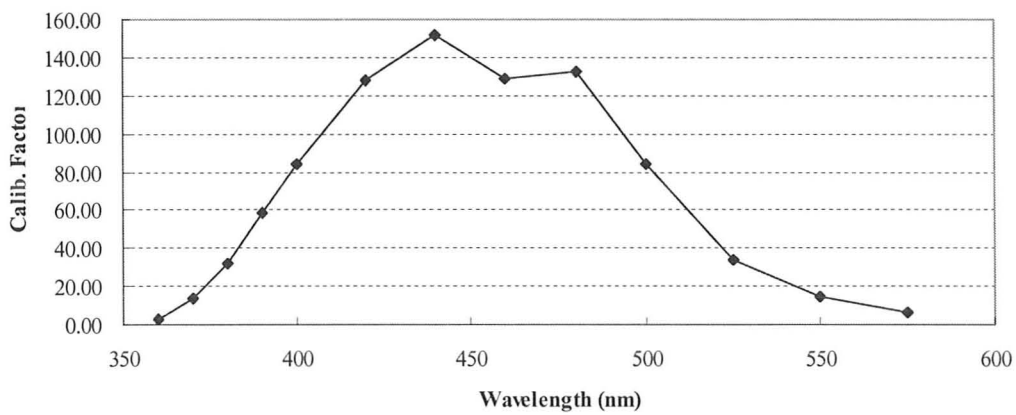
Fig. 4.7. Spectral correction function of the tr-LIFS system

Figure 4.8. illustrates the communication structure implemented for the calibration procedure.

The RF signal to the AOTF was modulated by the pulse generator to make the continuous wave

broadband light pulsative. The same modulation pulses were sent to the oscilloscope as a

waveform record trigger reference. A low-noise current preamplifier (SR570, Stanford Research

Systems, Sunnyvale, CA) was put in the system for signal amplification.
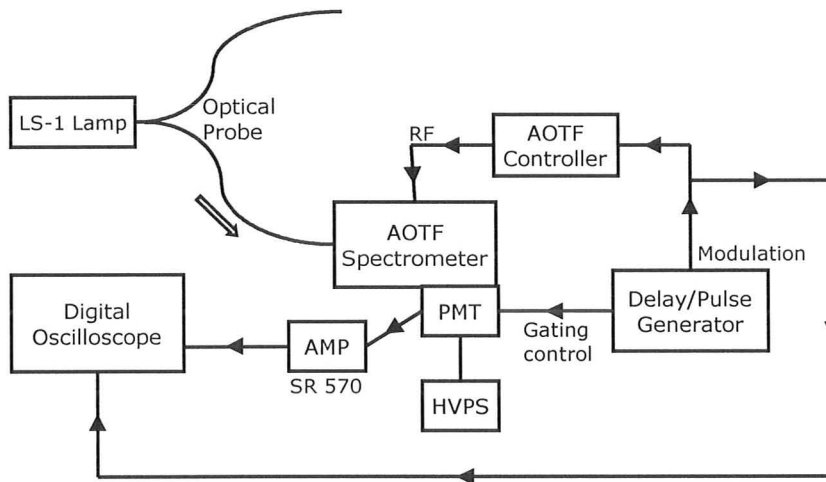
Fig. 4.8. Schematic of the spectral intensity calibration setup.

It turned out, however, that the correction function does not produce desirable

corrected emission spectra of the standard dyes with which the system was tested. It is

speculated that one critical problem lies with the AOTF controller. It was later found by

graphing the spectrum magnitude using spectral analysis function on the digital oscilloscope

that the RF the controller sent to the AOTF was always contaminated with unwanted

frequencies. Especially when the light intensity is low, the wavelength peaks produced by the

unwanted RFs would significantly contribute to the total light intensity of the diffracted light

measured by the PMT resulting in overestimations.

4. 3. Linearity of signal amplification

A nonlinear response of the PMT can result from an excessive current being drawn

from the photocathode. The linearity of signal amplification was determined by evaluating the

distortion of the amplified output signal as a function of input signal to the amplifier. The

emission decay from 10^{-3} M 9-CA (9-Cyananthracen 97%, 15,276-5, Aldrich) in ethanol

solution was used as an optical signal source. The AOTF filtering wavelength was set at 440 nm

where the optimal signal strength was acquired. The amplitude of the amplifier's input was

varied by gain adjustment of the MCP-PMT through changes of the high voltage from 1.45 to

2.11 kV. The corresponding peak-to-peak amplitude of the output signal displayed on the

oscilloscope varied from 2 mV to 2.8 V. 100 pulses were averaged for each signal acquisition. It

was found that the output signal amplitude has to be kept less than 2 V to safely avoid nonlinear

distortion. The measurement results are presented below.
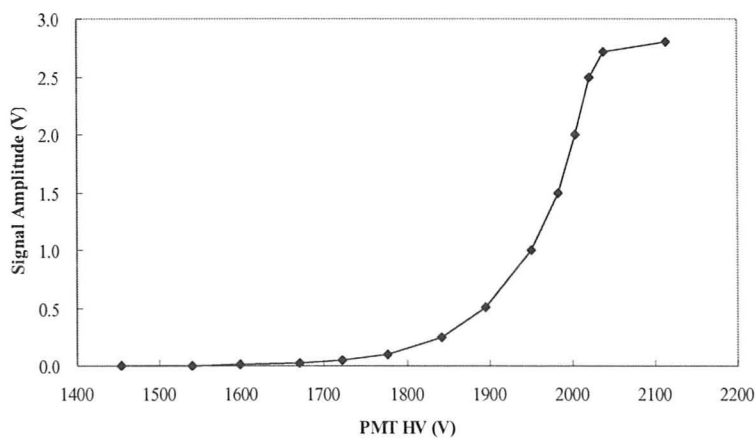
Fig. 4.9. Output signal amplitude vs. PMT high voltage.
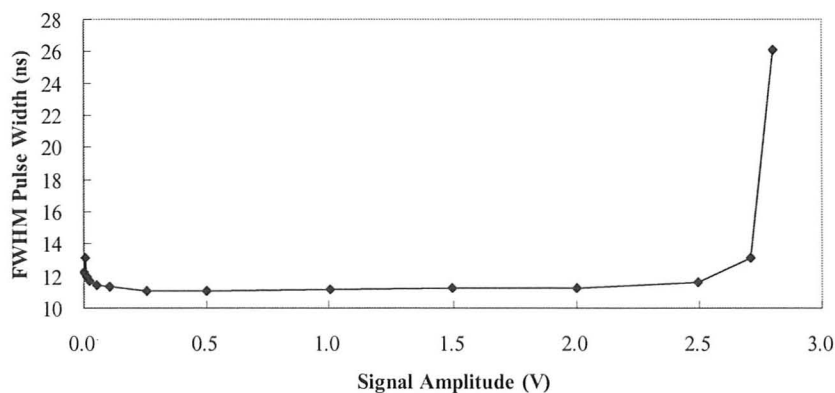
Fig. 4.10. Pulse width (FWHM) vs. amplitude of output signal.

4. 4. Sensitivity

The sensitivity of the system was determined by measuring the fluorescence emission

of 9-CA dissolved in methanol with gradually decreasing concentrations. The maximum

emission of the 9-CA solution was found at 436 nm. Therefore, the AOTF tuning wavelength

was set at 436 nm to allow as much light as possible to reach the PMT. For each concentration,

40 emission pulses were collected and averaged. The PMT voltage was kept constant at 2095V.

Tab. 4.3. shows the calculated SNR and lifetimes at different 9-CA concentrations. The lowest

9-CA concentration that yielded measurements with a SNR that allows acquisition of an

accurate lifetime was 2.5×10^{-7} at PMT of 2.095KV.

The overall system sensitivity depends on the PMT high voltage setting. Typically, the

sensitivity will improve with the increase of the PMT voltage. However, system noise will also

increase as well. As indicated in Fig. 4.10., the amplification of the signal will saturate at certain

high voltage settings. Additionally, when SNR is below 24, significant error in lifetime

calculation will arise (Table 4.3.).

Table. 4.3. Sensitivity measurement at 2.095KV

9-CA solution concenstraion (M)	SNR	Lifetime (ns)
10^{-4}	478	11.05
10^{-5}	338	11.21
10^{-6}	117	11.38
5×10^{-7}	58	11.33
2.5×10^{-7}	24	10.84
10^{-7}	13	4.52

4. 5. Dynamic range

The dynamic range is defined as the ratio of maximum and minimum concentration

where the lifetime estimation is accurate at certain PMT high voltage setting. As shown in Table

4.3., the dynamic range of the system is about 3 decades at 2.095KV.

4. 6. Throughput

Paratellurite performs exceptionally well in terms of AOTF diffraction efficiency. It

can outperform other birefringent materials by as much as a factor of ten. In the best case, the

efficiency of a TeO_2 AOTF system can be as high as 90% when a polarized input source is used

[2]. For unpolarized input light, it is the usual case to use only one first diffraction order for a

noncollinear TeO_2 AOTF, which results in low light throughput compared to grating-based

systems. In our AOTF setup, however, two first order diffraction beams are collected for

unpolarized input light to improve the overall throughput of the AOTF-based spectrometer. In

addition, the AOTF with a 5mm × 6mm optical aperture has an advantage over the

monochromator since the throughput is governed by the optical aperture as well as the diffraction efficiency. The throughput of the AOTF spectrometer was compared to that of a grating-based (monochromator) spectrometer by measuring a collimated laser beam of the pulsed diode laser (LDH-405, PicoQuant, Berlin, Germany) at 406 nm. For the grating-based spectrometer, the laser beam was focused onto the entrance slit of the monochromator (M-74100, 1200l/mm grating blazed at 350nm, Newport, Stratford, CT) via F/# matched lens. The input slit of the monochromator was set at 2.5 mm and the output slit was set at 0.9 mm. Figure 4.11. illustrates the measurement setup. The laser power was 338 μW before entering the spectrometers and the output light was measured using an optical power meter (1830-C, Newport). Both spectrometers were scanned across a wavelength range from 400 to 410 nm with a 0.2 nm increment. The results are shown in Figure 4.12. The AOTF-based spectrometer has comparable throughput at 406 nm to the grating-based spectrometer when the bandwidths of both systems were made similar.
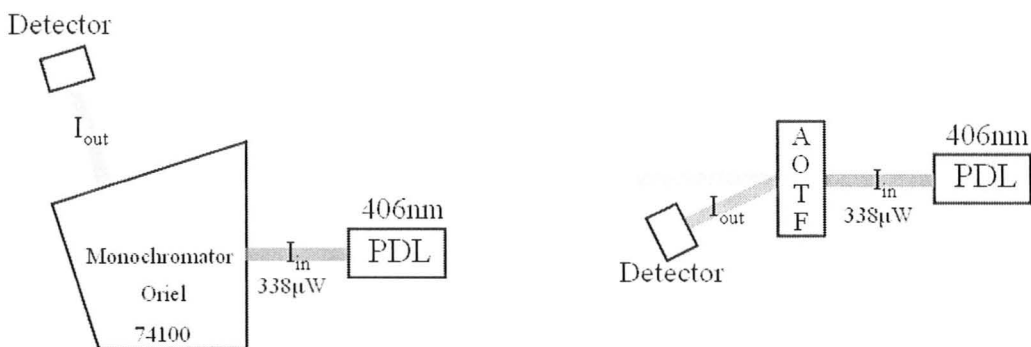
Fig.4.11. Throughput measurement setup for monochromator and AOTF.
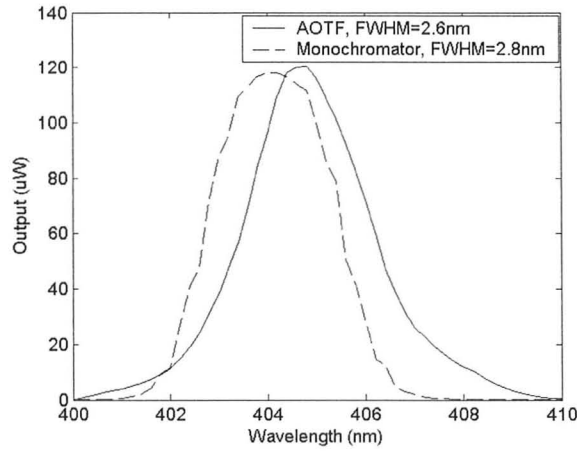
Fig. 4.12. Throughput measurements at 405 nm for monochromator and AOTF.

The throughput changes with incident wavelength due to the spectral dependence of the diffraction efficiency. Figure 4.13. shows the roughly estimated diffraction efficiency curve of the AOTF. The efficiency level substantially varies within the spectral range of interest whereas the efficiency of the monochromator (Figure 4.14.) does not significantly change as a function of wavelength.
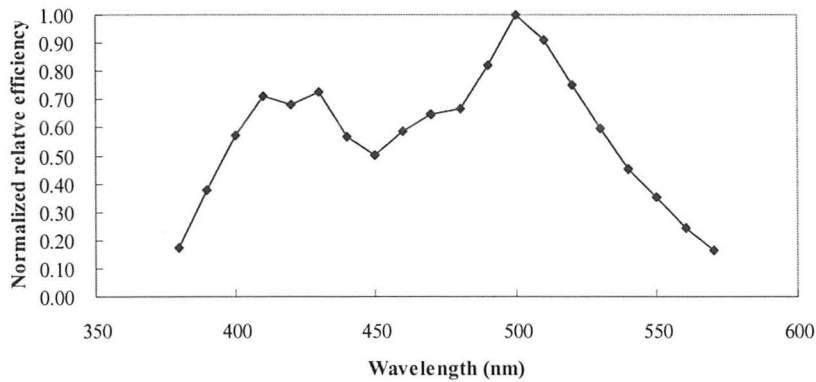
Fig. 4.13. Normalized spectral diffraction efficiency of the AOTF. The spectrum of combined diffraction beam at each wavelength was integrated over 6 nm range and divided by the corresponding integrated value of the broadband input light source spectrum.
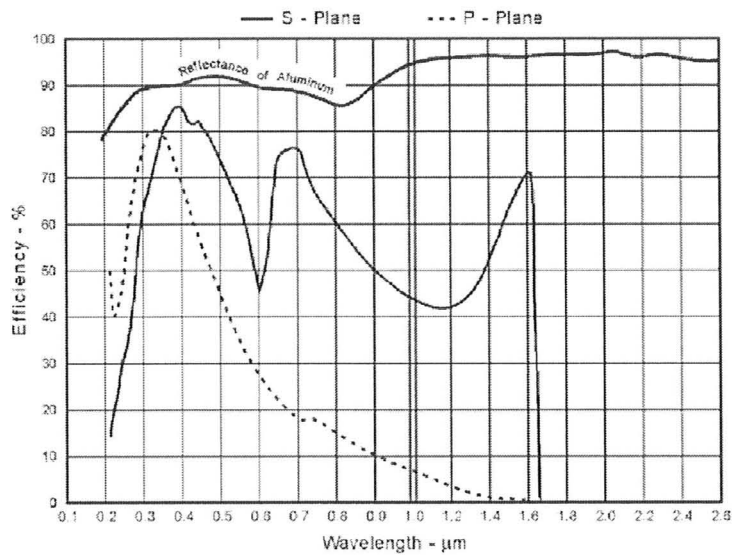
Groove Frequency:	1200 g/mm		Nominal Blaze Angle:	14°
Grating Type:	Plane Ruled		Blaze Wavelength:	400 nm
Coating:	Aluminum		Maximum Ruled Area:	102 x 128 nm
Remarks:	Measured under near-Littrow conditions.			

Note: Efficiency curves shown are relative (not absolute), are only representative, and can vary significantly depending on use geometry and measurement technique. Two masters with the same catalog number may have different efficiency curves. The uncertainty band on the data in the above relative efficiency curve(s) is +/- three percentage points. Maximum Ruled Area is expressed as L x W, where L is the length of the grooves and W is the ruled width.

Fig. 4.14. Spectral efficiency of the Spectra-Physics Oriel monochromator.
(adapted from the Newport website [6])

4. 7. Temporal response

The time response of a detector is not crucial for steady-state measurements. However, it is important to consider the detector time response for lifetime measurements. Typical tissue endogenous fluorophores have radiative lifetimes in the scale of a few hundred picoseconds to less than a few hundred nanoseconds. A temporal resolution of less than a few hundred picoseconds is required for a tr-LIFS system to accurately measure fluorescence lifetimes of tissue endogenous fluorophores [5]. One strong advantage of using a MCP-PMT is that it has tenfold smaller transit time spreads than other standard PMTs due to very little variation of

electron trajectory within the microchannel plate [7]. The temporal response of the entire system was characterized by measuring the pulsewidth of a narrowband 406 nm pulsed diode laser (PDL) and a wider band Nd:YAH 355 nm laser. The PDL has a pulsewidth of 60 ps while the Nd:YAH has a pulsewidth of about 350 ps. The temporal response for the PDL and Nd:YAG laser were 382±16 ps and 711±28 ps, respectively. It is necessary to verify the temporally resolving ability of the system by accurately retrieving subnanosecond fluorescence lifetimes.

4. 8. Validation of System Performance

The fluorescence data acquisition capability of the tr-LIFS system was validated by measuring fluorescence emission of several fluorophores with well-established characteristics.

4. 8. 1. Deconvolution

To retrieve the true lifetime of a fluorescence decay, optical distortions involved in the measurements by the instrument have to be reversed. This process is called deconvolution. The measured intensity decay of a fluorophore is a convolution with the lamp function. The task is to find the impulse response function that best matches the experimental data, which is what would be observed with perfect δ–function excitation. It is impossible to directly measure the impulse response function since the excitation cannot be a δ–function in the real world. However, we can consider the excitation to be a series of infinitely many δ–functions with varying amplitudes. Each of these δ–functions excites an impulse response from the fluorescent

sample with an intensity proportional to the amplitude of the δ–function. The measured function

can be regarded as the sum of all these decays starting with different amplitudes and times [7].

The convolution integral can be formulated as follows [8].

Let $I_E(t)$ = true intensity-time dependence of the excitation,

         $I_L(t)$ = measured intensity-time dependence of the excitation

                     distorted by the detector,

         $I_D(t)$ = fluorophore decay distorted by the excitation,

         $I_F(t)$ = measured fluorophore decay distorted both by the excitation and detector,

                     = output of the measuring instrument,

         $G(t)$ = δ-pulse response of the fluorophore,

                     = impulse response function (true fluorophore decay),

         $R(t)$ = δ-pulse response of the detector.

By the superposition principle, the following relationships in transform space can be
established.

$i_L(s) = r(s)\, i_E(s),$ $i_D(s) = i_E(s)\, g(s),$ $i_F(s) = i_D(S)\, r(s)$ [Eq. 4.8.]

$$\text{where for example, } i_L(s) = L\{I_L(t)\} = \int_0^\infty e^{-st} I_L(t) dt$$

It follows that $i_F(s) = g(s)\, i_L(s),$ [Eq. 4.9.]

and finally we get the convolution integral $I_F(t) = \int_0^t G(t')I_L(t - t')dt'$.   [Eq. 4.10.]

After $I_F(t)$ and $I_L(t)$ are measured by the instrument, the impulse response function G(t) can be

retrieved by a multiple exponential deconvolution algorithm and fluorescence lifetimes can be

estimated. In this technique, the impulse response function is assumed to be a multiple

exponential decay function and the goodness of fit is monitored by testing the randomness and

autocorrelation of residuals. The fluorescence lifetime is the time at which the impulse response

function decays to $1/e$ of its peak amplitude [5].

4. 8. 2. Fluorescence lifetime standards

Fluorescence of two standard dyes, 9-cyanoanthracene (9-CA: 152765, Sigma-Aldrich) and fluorescein (46955, Sigma-Aldrich), were measured. Both fluorescent dyes were dissolved in ethanol at a concentration of 10^{-4} M. A mixture solution was made of 10^{-4} M fluorescein and diluted 10^{-5} M 9-CA. Fluorescence decays of the pure and mixed dye solutions were measured across a wavelength range from 370 to 570 nm at 5 nm increments. Data acquisition time for the measurements across the 200 nm wavelength range at 5 nm increment was within 4 s. Time-integrated (steady-state) fluorescence spectra was obtained by integrating each fluorescence decay over the duration time. Fluorescence lifetime was calculated for each decay pulse using the multiple exponential deconvolution algorithm. Figure 4.15. and 4.16. show the time-integrated fluorescence spectra and lifetimes across the main emission spectral ranges of 9-CA and fluorescein, respectively. The emission peaks were at 435 nm for 9-CA and at 510 nm for fluorescein. Fluorescence lifetime was found to be almost constant over the emission spectra for both dyes. The averaged lifetimes over the emission spectra were 10.8±0.23 ns for 9-CA and 4.09±0.16 ns for fluorescein, which are in good agreement with the literature values [9-11]. The time-integrated fluorescence spectrum of the mixture solution shows two well separated emission peaks corresponding to the maximum emission of 9-CA and fluorescein. Fluorescence lifetimes (shown as dashed lines in the figures) were also well distinguished. The lifetime below

470 nm is dominated by 9-CA while above 500 nm it is attributed to fluorescein. These measurements are a good example showing that the AOTF-based time-resolved fluorescence spectrometer is capable of acquiring both spectral and lifetime information across entire fluorescence spectra with very short data acquisition time (less than 4 s).
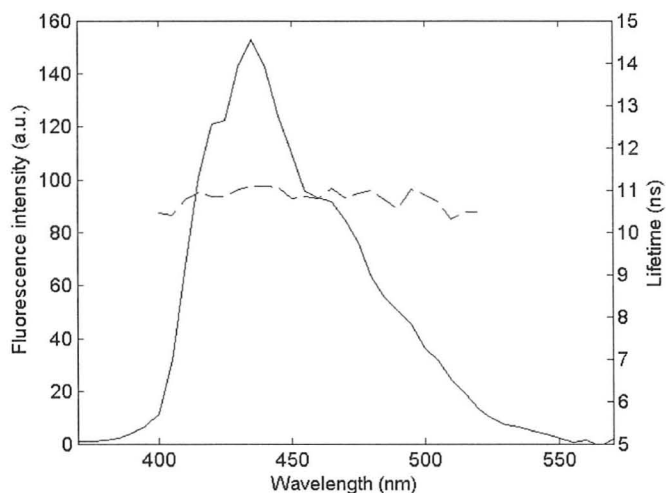
Fig. 4.15. Time-integrated fluorescence emission spectrum of 10^{-4} M 9-CA solution. Dashed line indicates estimated lifetimes.

Fig. 4.16. Time-integrated fluorescence emission spectrum of 10^{-4} M fluorescein solution.
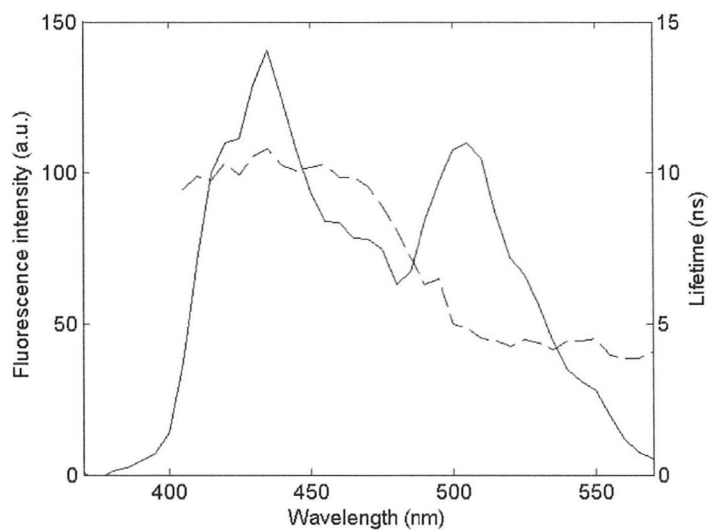
Fig. 4.17. Time-integrated fluorescence emission spectrum of mixture solution of 10^{-4} M fluorescein and 10^{-5} M 9-CA.

4. 8. 3. Fluorescent bio-molecules

To demonstrate the system performance with biological fluorophores typically found in human tissue, fluorescence lifetimes of reduced nicotinamide adenine dinucleotide (NADH, Sigma-Aldrich) and flavin adenine dinucleotide (FAD, Sigma-Aldrich) dissolved in phosphate buffered saline (pH 7.0) at a concentration of 10^{-4}M were measured to be 0.31±0.02 ns and 2.47±0.07 ns, respectively. These retrieved lifetimes agree well with reported values [5].
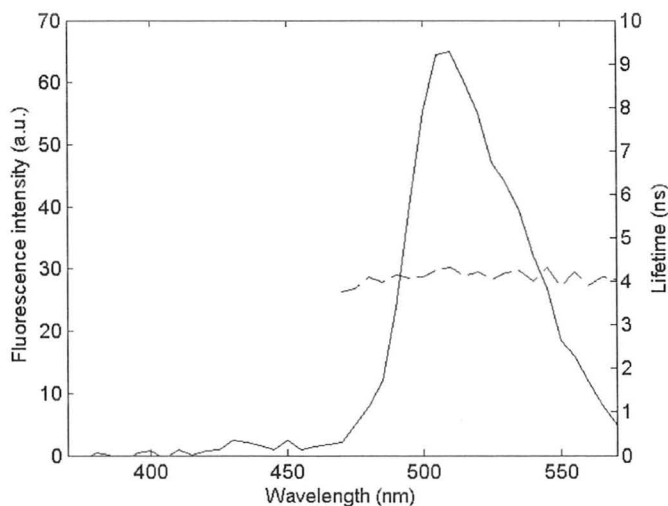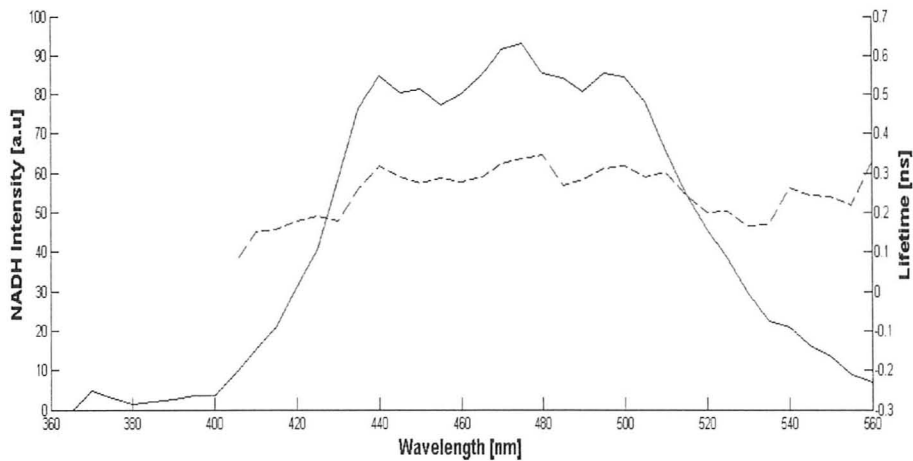
Fig. 4.18. Time-integrated fluorescence emission spectrum of 10^{-4} M NADH solution.
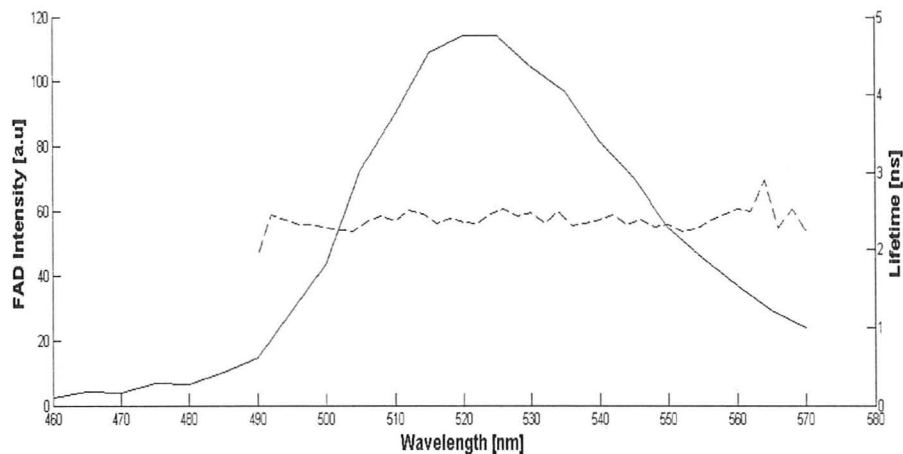
Fig. 4.19. Time-integrated fluorescence emission spectrum of 10^{-4} M FAD solution.

References

1. G. Georgiev, D. A. Glenar, and J. J. Hillman, *Spectral characterization of acousto-optic filters used in imaging spectroscopy*, Applied Optics, **41**(1), 209-217 (2002).

2. L. Bei et al, *Acousto-optic tunable filters: fundamentals and applications as applied to chemical analysis techniques*, Progress in Quantum Electronics, **28**, 67-87 (2004).

3. G. Georgiev, L. Konstantinov, *Design of the bandpass width, the spectral resolution and the diffraction efficiency of a non-collinear acousto-optic tunable filter of TeO_2*, Optics and laser technology, **27**, 383-387 (1995).

4. *OSM-400 Series Spectrometers User's Manual*, Newport.

5. Q. Y. Fang, T. Papaioannou, J. A. Jo, R. Vaitha, K. Shastry, and L. Marcu, *Time-domain laser-induced fluorescence spectroscopy apparatus for clinical diagnostics*, Review of Scientific Instruments, **75**(1), 151-162 (2004).

6. Newport website.

7. J. R. Lakowicz, *Principles of fluorescence spectroscopy*, 3rd ed., Springer (2006).

8. W. R. Ware, L. J. Doemeny, and T. L. Nemzek, *Deconvolution of Fluorescence and Phosphorescence Decay Curves. A Least-Squares Method*, The Journal of Physical Chemistry, **77**(17), 2038-2048 (1973).

9. J. A. Jo, Q. Y. Fang, T. Papaioannou, and L. Marcu, *Fast model-free deconvolution of fluorescence decay for analysis of biological systems*, Journal of Biomedical Optics, **9**, 743-752 (2004).

10. K. Vishwanath, W. Zhong, M. Close, and M. A. Mycek, *Fluorescence quenching by polystyrene microspheres in UV-visible and NIR tissue-simulating phantoms*, Optics Express, **14**, 7776-7788 (2006).

11. L. Z. Wang, Y. F. Shao, J. L. Zhang, and M. Anpo, *Study on the fluorescence properties of fluorescein dye incorporated into SBA-15*, Optical Materials, **28**, 1232-1234 (2006).

5. Discussion

We have developed an AOTF-based time-resolved fluorescence spectrometer (AOTF-TRFS) capable of acquiring time-resolved fluorescence spectra with high data acquisition speed apt for real-time clinical diagnostic applications. The system performance was evaluated by measuring the emission of fluorescence standard dyes and typical tissue fluorophores. The emission peaks in the time-integrated spectra and the retrieved lifetimes are in reasonable agreement with literature values over the desired spectral region between 370 nm and 550 nm. The cause of discrepancies between our measurements and the reported values may be attributed to different purification and preparation methods. We also demonstrated the system's ability to spectrally and temporally resolve mixed fluorophores.

One of the primary objectives in this work was to minimize data acquisition time. In this aspect, a critical improvement over the previous grating-based model was achieved. To acquire time-resolved fluorescence spectra between 370 nm and 550 nm at 5 nm increments, the AOTF-TRFS needs about 4 s while the grating-based system needs about 40s. For optical biopsy applications, there are multiple tissue components that are contributing to the overall fluorescence signal. Measuring fluorescence lifetime at multiple wavelengths across the spectral region of interests is particularly necessary in research studies searching for diagnostic signatures. A major obstacle preventing time-resolved fluorescence spectroscopy techniques

from in-vivo studies is the lengthy data acquisition time, which is incompatible to clinical procedures. Although the first generation system's 40 s acquisition time allows pilot clinical studies, it is not realistic to use it for large clinical trials. Hence, it is critical to further develop TRFS techniques with much shorter data acquisition time. The significantly reduced data acquisition time enables the AOTF-TRFS instrument to conduct near real-time clinical studies. This high data acquisition speed was mainly due to the use of AOTF technology. The wavelength switching speed of a monochromator is limited by the mechanical grating rotation, typically in the millisecond regime, which is much slower comparing to the microsecond time switching time of the solid-state AOTF. In addition, several other factors in our design also contributed to the improved data acquisition speed: 1) higher repetition rate of the Nd:YAG laser (50 Hz vs. 1kHz); 2) advanced fast frame features of the digital oscilloscope that can fetch and temporarily save a sequence of frames in the digitizer's internal memory; and 3) fully functional computer integrated inside the oscilloscope, which eliminated the need to move large amounts of data from the oscilloscope to an external host computer.

Comparing to grating-based monochromators, AOTF is not typically used in spectroscopy mainly due to its limited operating spectrum and low throughput (~40%) for randomly polarized light [1]. We have implemented a novel design that uses both first order diffracted beams that doubles the overall throughput. We have verified that, at 405 nm, the non-

collinear AOTF using both first diffraction order beams has comparable light throughput to a grating based monochromator. Since the AOTF in our system is optimized for only one diffraction order, however, using both diffraction beams gives rise to slight broadening of the spectral bandwidth. The AOTF may exhibit somewhat lower throughput at other wavelengths as its diffraction efficiency has stronger spectral dependence than a grating in the wavelength range of interest. Although the AOTF's operting spectral region is between 380-550 nm, which is much narrower than a typical monochromator, it still sufficiently meets the requirement for tissue diagnostics as most tissue endogenous fluorescence falls within that range.

The spectral resolution of the second generation AOTF-TRFS is much lower than the first generation grating based instrument. The spectral bandwidth of the AOTF is governed by many factors including incident angle, degree of collimation, and polarization. A better collimated beam can reduce the bandwidth and increase the throughput of the AOTF. The spectral resolution of a grating-based system largely depends on the groove spacing as well as the entrance and exit slit widths of the monochromator. Enhancing spectral resolution by decreasing slit widths comes with a trade-off because signal intensity will be reduced. The previous model has an adjustable spectral resolution between 0.5 and 10 nm, while mostly operated at 2 nm [2]. The AOTF-TRFS' spectral resolution of 2~3 nm between 380 ~ 550 nm is acceptable for measuring tissue endogenous fluorescence with 25 nm or wider broad emission

band.

Temporal response of the system is determined collectively by the response time of the photo detector (MCP-PMT), the amplifier, the digital oscilloscope, the stability of the laser and the trigger mechanism. The component with the highest temporal response is the digital oscilloscope with high sampling rate (40 GHz for single channel) and analog bandwidth (2.5GHz). This is a noteworthy improvement over the first generation system, where the 1GHz bandwidth oscilloscope is the slowest component. Both the photo detector and the amplifier are the same as in the first generation system. Although the pulse width of the Nd:YAG laser (300 ps) is much shorter than the nitrogen laser used in the 1st generation system (700 ps), there is no considerable improvement in its pulse width stability. In addition, the built-in optical trigger is much more unstable than the one in the nitrogen laser. Therefore, there is no substantial improvement in temporal response between the first and the second generation systems.

The system temporal response was characterized by measuring the well-characterized subnanosecond lifetime (nearly delta function decay) of NADH. The calculated lifetime of NADH was 0.31 ns, which is in good agreement with the values reported in literature. The temporal resolution of our tr-LIFS system must be sufficient for measuring lifetimes of subnanosecond or longer fluorescence decays of most biological probes.

There is more room for improvement in the current, 2nd generation TRFS system. We have spent a lot of time in optimizing the collimation of the collection fiber since the degree of collimation determines the diffraction efficiency and bandwidth of the AOTF spectrometer. The propagation profile of emission light from the fiber probe is very complex mainly due to the fact that the emission channel of the probe is consisted of 12 individual fibers. Two fiber cores farthest from each other are separated by about 0.8 mm. A visible portion of emission light does not pass through the AOTF aperture and is blocked by the crystal housing. Since the aperture is fully filled with light, there may be more diffraction and more amount of light scattering from the crystal surfaces that contributes to background noise than when the diameter of the collimated beam at entrance is smaller than the aperture. An improved collimation state (smaller diameter and divergence angle) will lead to higher SNR of collected data. This may be achieved by using a customized microlens array or a gradient index (GRIN) lens, for example.

For rapid screening of a large area of skin, an imaging modality that can quickly obtain information about the overall complex skin topology will be more practical than a point monitoring strategy. The AOTF technology has been in use for hyperspectral imaging (HSI) applications where spectroscopic information is rendered in 2D image form. The AOTF's large aperture and high spatial resolution allows optical images from an imaging fiber optic probe to be recorded by the charge-coupled device (CCD) imager. The HSI system can be designed for

dual-modality diagnostics to detect both fluorescence and diffuse reflectance images [3]. It will

be a great optical challenge if both first order diffraction beams are to be used to increase

throughput for imaging as the resulting image quality will be extremely sensitive to the spatial

synchronization of two separate images.

References

1. L. Bei et al, *Acousto-optic tunable filters: fundamentals and applications as applied to chemical analysis techniques*, Progress in Quantum Electronics, **28**, 67-87 (2004).

2. Q. Y. Fang, T. Papaioannou, J. A. Jo, R. Vaitha, K. Shastry, and L. Marcu, *Time-domain laser-induced fluorescence spectroscopy apparatus for clinical diagnostics*, Review of Scientific Instruments, **75**(1), 151-162 (2004).

3. T. Vo-Dinh, B. Cullum and P. Kasili, *Development of a multi-spectral imaging system for medical applications*, Journal of Physics D: Applied Physics, **36**, 1663-1668 (2003).